



26 **Abstract:**

27 Coronaviruses (CoV), such as severe acute respiratory syndrome coronavirus (SARS-CoV) and  
28 Middle East respiratory syndrome coronavirus (MERS-CoV), are of medical importance with high  
29 mortality rates and significant zoonotic and pandemic potential. Here, we apply ribosome profiling  
30 and parallel RNASeq to globally analyse changes in the host cell translatome and transcriptome  
31 upon infection with mouse hepatitis virus, strain A59 (MHV-A59), a model murine coronavirus in  
32 the same genus as SARS-CoV and MERS-CoV. We observed translational upregulation of ATF4,  
33 ATF5 and Ddit3 and activation of the unfolded protein response (UPR). Phosphorylation of eIF2 $\alpha$   
34 led to the global inhibition of translation and a substantial increase in empty 80S ribosomes. A drug  
35 that inhibits the UPR attenuates virus growth suggesting that MHV may have evolved to subvert the  
36 UPR to its own advantage. We also investigated an artefact of cycloheximide pretreatment in  
37 ribosome profiling whereby ribosomes accumulate at the 5' end of coding sequences in stressed  
38 cells but not in unstressed or untreated cells, thus extending earlier studies in yeast to mammalian  
39 cells. The study sheds light on the mechanisms of CoV translational shutoff and reveals a potential  
40 new therapeutic strategy.

41

42 **Author Summary:**

43 Ribosome profiling is an emerging technique that reveals a global snap shot of protein synthesis by  
44 precisely mapping the positions of translating ribosomes. It has particular applicability to virology  
45 where it allows not only monitoring of viral gene expression, but also host response at the level of  
46 individual genes and globally. In this work, we use ribosome profiling and parallel transcriptome  
47 sequencing (RNASeq) to monitor changes in transcription and translation in cells infected with the  
48 model coronavirus, murine coronavirus strain MHV-A59, a virus in the same genus as the  
49 medically important SARS-CoV and MERS-CoV. The sensitivity and precision of the approach  
50 permit us to obtain a high-resolution analysis of different biological processes – such as the  
51 activation of the unfolded protein response. At late time points of infection, translation is inhibited  
52 globally and, surprisingly, viral transcripts are not resistant to this effect. Nonetheless, relief of  
53 translational inhibition with a drug that interferes with the unfolded protein response is detrimental

54 to virus replication. This study sheds new light on the complex interactions between virus and host  
55 during infection and provides new potential targets for antiviral intervention.

56

57 **Introduction:**

58

59 The *Coronaviridae* are a family of enveloped viruses with positive-sense, monopartite, single-  
60 stranded RNA genomes. At 27–32 kb, coronaviruses (CoVs) have the largest known RNA  
61 genomes. CoVs cause a broad range of diseases in animals and humans, ranging from the common  
62 cold to severe acute respiratory syndrome (SARS) [1]. Amongst CoVs of medical importance with  
63 high mortality rates and pandemic potential are SARS-CoV and MERS-CoV, both members of the  
64 genus *Betacoronavirus*. Murine coronavirus, a betacoronavirus more commonly referred to as mouse  
65 hepatitis virus (MHV), has been used as a model to study the replication and biology of other  
66 members of the genus.

67

68 Virus infection alters cellular gene expression to facilitate replication of the viral genome and the  
69 assembly of virus particles. As with all viruses, CoVs rely on the host cell translational machinery  
70 for viral protein synthesis. Many viruses have evolved mechanisms to shut-off host mRNA  
71 translation, which can increase the availability of the translational machinery for non-canonical  
72 modes of viral protein synthesis, and at the same time inhibit host antiviral responses [2]. Exactly  
73 how CoVs induce host translational shut-off and its significance in relation to the synthesis of virus  
74 proteins, particularly at later times of infection, is still poorly understood.

75

76 During CoV replication, the massive production and modification of viral proteins, as well as virion  
77 budding-related endoplasmic reticulum (ER) membrane depletion, can lead to overloading of the  
78 folding capacity of the ER and, consequently, ER stress [3]. This activates the unfolded protein  
79 response (UPR) which returns the cell to homeostasis and mitigates the major risk that protein  
80 misfolding poses for correct cellular function [4]. In mammalian cells, the UPR is controlled by  
81 three ER-resident transmembrane sensors: the inositol-requiring enzyme-1 (IRE1), the PKR-like ER  
82 kinase (PERK), and the activating transcription factor-6 (ATF6). These sensors recognize  
83 unfolded/misfolded proteins inside the ER and transmit a signal to the nucleus to transcribe specific

84 genes whose products act to lower protein synthesis and increase ER folding capacity [4]. Previous  
85 studies (reviewed in [5]) have aimed to establish how the different UPR pathways are involved  
86 during CoV infection.

87

88 Ribosome profiling (RiboSeq) allows global monitoring of cellular translation by mapping the  
89 positions of translating ribosomes on the transcriptome [6-8]. RiboSeq reveals the location and  
90 abundance of ribosomes on specific mRNA species with single-nucleotide precision. In conjunction  
91 with RNASeq, to determine the corresponding transcriptome, RiboSeq has been used to elucidate  
92 changes in translation, transcription and translation efficiency in viral and host gene expression  
93 during the course of infection [9-19].

94

95 Here, we use RiboSeq and parallel RNASeq to globally analyse changes in the host translatome and  
96 transcriptome throughout a time course of CoV infection. We observe activation of different  
97 pathways of the UPR leading to eIF2 $\alpha$  phosphorylation and translational shut-off at the level of  
98 initiation which we confirm by polysome profiling. Surprisingly, however, a pharmacological  
99 inhibitor of the UPR was found to attenuate virus replication. We also investigate a remarkable  
100 perturbation in ribosome footprint distributions on coding sequences previously observed at late  
101 time points of infection and determine that it is a methodological artefact arising from the use of the  
102 elongation inhibitor cycloheximide. This detailed analysis of cellular translation during MHV  
103 infection provides new insights into the mechanism of CoV translational shutoff and the complex  
104 interactions between virus and host during infection, and may aid the identification of new targets  
105 for antiviral intervention.

106

## 107 **Results:**

108

### 109 **Effects of MHV-A59 infection on cellular gene expression**

110 To survey genome-wide changes in host translation and transcription during CoV-infection, we  
111 interrogated sequencing data generated previously in this laboratory [16]. In these experiments, we

112 generated RNASeq and RiboSeq data from two independent biological repeats of murine 17 clone 1  
113 cells (17 Cl-1) infected with recombinant MHV-A59 at a multiplicity of infection (MOI) of 10, and  
114 harvested at 1, 2.5, 5 and 8 h post-infection (p.i.), with mock-infected cells harvested at 1 and 8 h.

115

116 To assess the effects of MHV infection on cellular transcript abundance, differential expression  
117 analyses were performed with DESeq [20], EdgeR [21], NOISeq [22] and BaySeq ([23]). The  
118 different analyses had a large number of overlapping predictions (Fig 1A). The volcano plot (Fig  
119 1B) derived from BaySeq analysis of four uninfected (1 and 8 h) and two infected (5 h p.i.)  
120 RNASeq libraries revealed that some of the most differentially expressed cellular transcripts (red  
121 points) are related to the host translational apparatus (*Eef1a1* – eukaryotic elongation factor 1A-1;  
122 *Eif3f* – eukaryotic initiation factor 3 subunit F; *Eif1* – eukaryotic initiation factor 1; *Eif2s3x* –  
123 eukaryotic initiation factor 2 subunit 3 gamma, and *Eif2b3* – eukaryotic initiation factor 2B GDP-  
124 GTP exchange factor subunit gamma), the UPR (*Herpud1* – homocysteine inducible ER protein  
125 with ubiquitin like domain 1 and *Chac1* – glutathione-specific gamma-glutamylcyclotransferase 1),  
126 and the gene coding for the largest subunit of RNA polymerase II, *Polr2a*.

127

128 To further validate changes in the transcript abundance of these genes, total RNA was extracted  
129 from three biological replicates of MHV-infected and mock-infected cells at 5 h p.i. and the levels  
130 of selected up-regulated (Fig 1C, left panel) and down-regulated (Fig 1C, middle panel) transcripts  
131 assessed by quantitative real-time PCR (qRT-PCR), normalized by a ‘housekeeping gene’,  
132 ribosomal protein L19 (RPL19), which has been reported to be unaffected by ER stress [24,25].  
133 qRT-PCR was also used to assess the abundance of viral nucleocapsid (N) transcripts (Fig 1C, right  
134 panel). Up-regulated transcripts had qRT-PCR values broadly consistent with the RNASeq  
135 measurements (Fig 1B and 1C) whereas down-regulated transcripts did not, with the exception of  
136 *Eef1a*. We note, however, that the *Rpl19* transcript is, in fact, moderately down-regulated at 5 h p.i.  
137 (relative to the global transcriptome mean) (Fig 1B, yellow), thus biasing the ratio quantifications.

138 A comparison of differential expression between the 1 and 8 h mocks showed much smaller  
139 differences, with only four transcripts having changes with a false discovery rate (FDR)  $\leq 0.05$   
140 (S1A Fig).

141

142 CoVs induce host translational shut-off [26-31] though the mechanisms have not been well-defined.  
143 We reasoned that some host genes may be resistant to virus-induced shut-off and that identifying  
144 such genes might give new insights into the shut-off mechanism(s). To evaluate differences at the  
145 level of translation as a result of MHV infection, we calculated relative translation efficiencies (TE)  
146 – defined herein as the ratio of ribosome-protected-fragment (RPF) and total RNA density in the  
147 coding region (CDS) of a given gene – at 5 and 8 h p.i. TE was estimated using Bayseq in the  
148 paired library mode, Babel [32] and Xtail [33]. These analyses had few overlapping predictions of  
149 genes significantly differentially expressed, with Xtail producing a much higher number of  
150 predictions (Fig 2). These differences are likely due to variations in model assumptions between the  
151 different approaches and reflect the greater difficulty inherent in modeling a quotient distribution  
152 (i.e. RiboSeq/RNASeq). To proceed, we focused on genes that showed more than a 2-fold  
153 difference in mean TE between infected and mock samples, and a FDR  $\leq 0.05$  (upper right and  
154 upper left quadrants; Fig 2B – Babel 5 h p.i.; Fig 2C – Xtail 5 h p.i. and Xtail 8 h p.i.). Translational  
155 differences between 1 and 8 h mock-infected cells are shown in S1B Fig.

156

157 Among the mRNAs found to be preferentially translated during MHV-infection were those whose  
158 translation is known to be induced by eIF2 $\alpha$  phosphorylation, including those for transcription  
159 factors ATF4 (activating transcription factor 4), ATF5 (activating transcription factor 5) and CHOP  
160 (DDIT3/GADD153) (Fig 2B and 2C; S2A Fig). The mRNAs encoding these proteins contain  
161 (multiple) inhibitory upstream open reading frames (uORFs) in their 5' leaders and undergo  
162 selective re-initiation of the main ORF under conditions of eIF2 $\alpha$  phosphorylation [34-39]. Another  
163 gene previously shown to be resistant to eIF2 $\alpha$  phosphorylation-induced translational attenuation is

164 Slc35a4 (Solute Carrier Family 35, Member A4; Fig 2B; [39]). In our study, the vast majority of  
165 RPFs derived from this mRNA mapped to the 102-codon uORF (S2B Fig). These results are  
166 consistent with eIF2 $\alpha$  phosphorylation (leading to inhibited initiation) being a major cause of host  
167 translational shut-off during MHV infection.

168

169 **An artefact of cycloheximide treatment explains a remarkable perturbation in the  
170 distribution of elongating ribosomes**

171 Previous meta-analyses of RPFs mapping to host mRNAs in MHV-infected cells indicated a  
172 remarkable perturbation in host cell translation at late time points [16] with a greatly increased  
173 proportion of reads mapping to the first ~30–40 codons of CDSs in MHV-infected cells at 5 and 8 h  
174 p.i. (e.g. Fig 3A compares 8 h p.i. with 8 h mock; data from [16]). Other ribosome profiling studies  
175 have revealed a similar accumulation of ribosomes in the 5' portion of CDSs after heat shock,  
176 proteotoxic and oxidative stress, and attributed this to an early post-initiation inhibition of  
177 elongation under cell stress [40-42]. More recently, these results have been called into question by  
178 the discovery that cycloheximide pre-treatment in yeast leads to an artefactual accumulation of  
179 ribosomes in the 5' portion of CDSs specifically in stressed cells [43,44]. Moreover, this  
180 accumulation was not seen if the yeast cells were flash frozen without cycloheximide pre-treatment,  
181 or if very high concentrations of cycloheximide were used.

182

183 In order to determine whether this experimental artefact might extend to stressed mammalian cells  
184 and perhaps explain the observed accumulation of ribosomes downstream of initiation sites during  
185 virus infection [16], 17 Cl-1 cells were infected with MHV A-59 at MOI of 10 and at 8 h p.i.  
186 harvested either by flash freezing in the absence of cycloheximide, or following supplementation of  
187 the growth medium with 100  $\mu$ g/ml cycloheximide (CHX 1X) or 10 mg/ml cycloheximide (CHX  
188 100X) for minutes prior to harvesting. A similar experiment was performed with 17 Cl-1 cells  
189 incubated with a pharmacological inducer of ER stress, tunicamycin, for 6 h which activates all

190 UPR signalling pathways. Ribosomal occupancy profiles and the effects of stress and drug  
191 treatment are shown in Fig 3B (for MHV-infected cells) and Fig 3C (for tunicamycin-treated cells).

192

193 A modest increase in ribosome occupancy downstream of initiation sites occurred in tunicamycin-  
194 stressed cells under normal cycloheximide treatment (compare “tunicamycin CHX 1X” with “mock  
195 CHX 1X” plots; Fig 3C). Similar to findings in stressed yeast cells [43], this could be alleviated by  
196 high concentrations of cycloheximide or flash freezing without cycloheximide pre-treatment (Fig  
197 3C, CHX 100X and “flash frozen” plots). In virus-infected cells, however, a much more  
198 pronounced accumulation of ribosomes was observed downstream of initiation sites under  
199 cycloheximide treatment, and this was not alleviated even when cycloheximide was used at 100-  
200 fold the normal concentration (Fig 3B, CHX 1X and 100X plots). However, this ribosome peak  
201 completely disappeared when cells were flash frozen without cycloheximide pre-treatment (Fig 3B,  
202 “flash frozen” plots). Thus we conclude that the cycloheximide-induced accumulation of ribosomes  
203 in the 5' region of CDSs also occurs in stressed mammalian cells and, further, that this effect is not  
204 necessarily negated simply by increasing the cycloheximide concentration.

205

206 As in previous studies [41,42], we quantified excess 5' ribosome density for individual transcripts  
207 by means of a 5' loading ratio statistic where we compared the density of RPFs in the 5'  
208 approximately 30 codons of each CDS to the density of RPFs in the 3' remainder of the CDS. As  
209 expected, when harvested at 8 h in the presence of cycloheximide the 5' loading ratios of  
210 cytoplasmic mRNAs showed a substantial increase in MHV-infected cells compared to mock-  
211 infected cells (Fig 4, left panel), whereas there was no such effect when cells were harvested with  
212 flash freezing (Fig 4, right panel). Interestingly, but not unexpectedly, this effect was not seen for  
213 mitochondrial mRNAs, which had similar 5' loading ratio statistics over all conditions (Fig 4, red  
214 crosses).

215 In view of the cycloheximide artefact, data from the flash frozen mock and MHV-infected samples  
216 were used for the individual gene plots shown in the following sections.  
217

## 218 **MHV infection and activation of the unfolded protein response**

219 The endoplasmic reticulum is the major site for synthesis and folding of secreted and  
220 transmembrane proteins. When protein synthesis surpasses the folding capacity, unfolded proteins  
221 accumulate and lead to ER stress. To return to homeostasis, cells have evolved the UPR [4]  
222 comprising three pathways that are initiated by three ER sensor proteins: PERK, ATF6 and IRE1.  
223 These sensors are transmembrane proteins with a luminal domain that recognizes  
224 unfolded/misfolded protein inside the ER, and a cytosolic domain that relays the signal to the  
225 nucleus in order to switch on specific downstream genes to lowering protein synthesis and  
226 increasing ER folding capacity. Similar to other viruses, CoV infection triggers cellular stress  
227 responses in infected host cells (reviewed in [5]). The close association of CoV replication with the  
228 ER during the formation of double-membrane vesicles (DMVs), the massive production and  
229 modification of structural proteins, and the depletion of ER membrane during budding, results in  
230 ER stress responses [3]. Therefore, CoVs must cope with translational shutoff in order to maintain  
231 viral protein production. Although several studies [29, 45-47] have aimed to establish how each of  
232 the three UPR sensor-pathways may be involved during CoV infection, we wanted to take  
233 advantage of the high-resolution that ribosome profiling can provide to analyse in detail each  
234 specific arm of the UPR response during MHV infection.

235

## 236 **Monitoring ATF6 and IRE1 $\alpha$ activity**

237 Upon induction of ER stress, ATF6 translocates from the ER to the Golgi apparatus where it is  
238 cleaved by the proteases Site-1 (S1P) and Site-2 (S2P) [48]. After cleavage, the amino-terminus of  
239 ATF6, containing a basic leucine zipper (bZIP) transactivating domain, translocates to the nucleus  
240 to upregulate the ER chaperone immunoglobulin heavy chain binding protein (BiP/Grp78). A

241 simple way to evaluate ATF6 activity is thus to measure BiP/Grp78 mRNA or protein levels. 17 Cl-  
242 1 cells were infected with MHV-A59 or incubated with tunicamycin. Cells were harvested at 2.5, 5,  
243 8 and 10 h p.i. and analyzed by qRT-PCR (Fig 5A). An induction of *BiP/Grp78* transcription was  
244 observed in tunicamycin-treated (purple) and MHV-infected cells (orange) from 2.5 to 8 h p.i.  
245 followed by a modest decline, whereas mock-infected cells (blue) showed no induction.  
246 Surprisingly, whereas Western blot analysis (Fig 5B) confirmed induction of Bip/Grp78 protein in  
247 tunicamycin-treated cells by 8 h p.i., no such induction was seen in MHV-infected cells.

248

249 At 8 h p.i., MHV-infected cells were harvested by flash freezing in the absence of cycloheximide.  
250 As a positive control for UPR activation, cells treated with tunicamycin for 6 h were also harvested  
251 by flash freezing. RNASeq and RiboSeq read counts of *BiP/Grp78* (Mock 8 h and MHV 8 h p.i.;  
252 Fig 5C) revealed an increase in RNASeq reads in MHV-infected cells (Mock RNA and Inf RNA  
253 panels) consistent with the qRT-PCR results. Although an expected increase in RPFs was seen (Inf  
254 Ribo panel), ribosome density was not as high in MHV-infected cells as in tunicamycin treated cells  
255 (Fig 5C, Tunica Ribo panel). A lower ribosome density in the *BiP/Grp78* ORF for MHV-infected  
256 cells likely explains why this protein was not immunodetected at later times of infection.

257

258 ER stress induction activates endonuclease IRE1 $\alpha$  which cleaves X-box binding protein-1 (*Xbp-1*)  
259 mRNA [49,50]. Activated IRE1 $\alpha$  removes a 26-nt intron from unspliced *Xbp-1* (*Xbp-1u*) mRNA  
260 leading to a translational reading frame shift and a longer protein. The product of spliced *Xbp-1*  
261 mRNA (*XBP-1s*) is an active transcription factor that upregulates the expression of ER-associated  
262 degradation (ERAD) components and ER chaperones. Determination of *Xbp-1* splicing was done by  
263 reverse transcriptase PCR (RT-PCR) of total RNA extracted from 17 Cl-1 cells infected with MHV-  
264 A59 or incubated with tunicamycin, using specific primers flanking the *Xbp-1* splice site (Fig 5D).  
265 At all timepoints, *Xbp-1u* was the predominant form in mock-infected cells whereas *Xbp-1s* was the  
266 major species in tunicamycin-treated cells. In virus-infected cells, *Xbp-1u* was predominant at 2.5 h

267 p.i. but *Xbp-1s* became predominant at 5 h p.i. In order to analyse translation of *Xbp-1u* and *Xbp-1s*  
268 in virus-infected cells, we inspected the ribosome profiling data (Fig 5E). For 8 h p.i. MHV-infected  
269 cells (Info Ribo panel) and tunicamycin-treated cells (Tunica Ribo), an increased number of reads  
270 mapped in the +2 reading frame (yellow peaks) of the *Xbp-1u* sequence, and downstream of the  
271 annotated stop codon. These reads result from translation of the *Xbp-1s* frameshifted isoform and  
272 indicate a dramatic increase in production of the active transcription factor.

273

274 **Monitoring PERK-eIF2 $\alpha$  -ATF4 activity**

275 In response to ER stress, PERK oligomerizes and auto-phosphorylates [51]. Activated PERK  
276 phosphorylates the  $\alpha$ -subunit of eukaryotic initiation factor 2 (eIF2 $\alpha$ ) which in turn impairs  
277 recycling of inactive eIF2-GDP to active eIF2-GTP resulting in a general shutdown of protein  
278 synthesis [52]. However, as previously described, translation of ATF4 is increased in this situation  
279 [34,35,53] leading to the induction of its target gene *Chop*. To monitor activation of this pathway,  
280 we analysed CHOP, ATF4 and p-eIF2 $\alpha$  expression by qRT-PCR and Western blotting. 17 Cl-1 cells  
281 were infected with MHV-A59 or incubated with tunicamycin for 2.5, 5, 8 and 10 h. As shown in  
282 Fig 6A, *Chop* mRNA levels (measured as the *Chop/RpL19* ratio) increased five-fold in  
283 tunicamycin-treated cells (purple) compared to mock-infected cells (blue), and were stable over the  
284 time course. In MHV-infected cells (orange), the ratio also increased from 2.5 to 8 h p.i. although  
285 not to the level seen in tunicamycin-treated cells. Protein expression was determined by  
286 immunoblotting using antibodies specific for ATF4, p-eIF2 $\alpha$  and N proteins with GAPDH and  
287 eIF2 $\alpha$  as loading controls (Fig 6B). ATF4 and p-eIF2 $\alpha$  were detected at all time points in  
288 tunicamycin-treated cells and all of the proteins were detected in MHV-infected cells from 5 h p.i.  
289 onwards. Subsequently, we analysed profiles of the RiboSeq and RNASeq reads mapping to ATF4  
290 in the virus-infected and tunicamycin-treated cells (Fig 6C). Consistent with previous studies  
291 [34,35], translation of the short (three codon) uORF1 (frame +2, nucleotides 399 to 407) was  
292 observed under all conditions. In mock-infected cells, uORF2 was efficiently translated (Mock Ribo

293 panel; reads in yellow mapping to uORF2 indicated by a yellow rectangle, frame +2) thus diverting  
294 scanning preinitiation ribosomes from accessing the main ORF (blue rectangle, frame 0, reads in  
295 purple) to which very few RPFs mapped. In contrast, in 8 h p.i. MHV-infected cells (Inf Ribo  
296 panel), a substantial fraction of preinitiation ribosomes were able to scan past uORF2 to translate the  
297 main ORF, leading to a reduced density of ribosomes on uORF2 and a greatly increased number of  
298 RPFs mapping to the main ORF. Tunicamycin-treated cells showed an intermediate ribosome  
299 distribution, but again with efficient translation of the main ORF.

300

301 Fig 6D displays the RiboSeq and RNASeq profiles for *Chop*. Consistent with the qRT-PCR analysis  
302 (Fig 6A), RNASeq reads (Inf RNA panel) were increased at 5 h p.i. compared to mock and there  
303 was an increase in the number of RPFs mapping to the main ORF (blue rectangle, purple reads).  
304 This increase in translation of the main ORF was also accompanied by an increase in the number of  
305 RPFs derived from ribosomes initiating on the *Chop* uORF (yellow rectangle, blue reads). This  
306 uORF occupancy was especially strong in tunicamycin-treated cells (Tunica Ribo panel).

307

### 308 **Polysome profiling of 17 Cl-1 cells infected with MHV-A59**

309 Since total read counts are normalized by library size, ribosome profiling does not provide  
310 information on total global translation levels. To further investigate virus-induced inhibition of  
311 translation as a consequence of UPR activation and eIF2 $\alpha$  phosphorylation, analytical polysome  
312 profiling (Fig 7A) was done for mock- and MHV-infected 17 Cl-1 cells. Cytoplasmic extracts were  
313 prepared in the presence of cycloheximide to retain intact monosomes and polysomes and analyzed  
314 by sucrose density gradient centrifugation. This revealed an accumulation of monosomes (80S) in  
315 MHV-infected cells from 5 h p.i. onwards, consistent with inhibition of initiation. To investigate  
316 whether the 80S ribosomes accumulating during MHV infection contain mRNA (as an indicator of  
317 a translating ribosome), polysome profiling was repeated using a higher salt buffer (400 mM KCl;  
318 Fig 7B), conditions in which 80S ribosomes lacking mRNA dissociate into constituent subunits. In

319 mock-infected cells, a modest diminution of 80S levels was observed at 400 mM KCl (mock 5 h,  
320 compare Fig 7A panel 2, and Fig 7B left panel), but a much greater reduction in 80S was observed  
321 in MHV-infected cells (MHV 5 h p.i., compare Fig 7A panel 5 and Fig 7B right panel), indicating  
322 that the vast majority of 80S ribosomes accumulating at this time point are not mRNA-associated.  
323 These data indicate that MHV-infection leads to translational shut-off via inhibited initiation,  
324 consistent with the effects of eIF2 $\alpha$  phosphorylation.

325

326 **Effect of the PERK inhibitor GSK-260614 on MHV replication**

327 GSK-260614 is a potent and selective high affinity ligand of the PERK kinase that interferes with  
328 kinase activity by competing for ATP [54,55]. In MHV-infected 17 Cl-1 cells at 5 h.p.i., the drug  
329 prevented phosphorylation of the PERK substrate, eIF2 $\alpha$ , in a dose-dependent manner (Fig 8A),  
330 effectively blocking this branch of the UPR, with only a minor effect on cell viability (S4A Fig).  
331 Pulse labelling of infected cells for one hour at 5 h.p.i. revealed, as expected, that prevention of  
332 eIF2 $\alpha$  phosphorylation increased modestly both viral (Fig 8A) and host protein synthesis (Fig 8B),  
333 without effect on mock-infected cells (Fig 8B).

334

335 Despite the increased virus protein synthesis, 17 Cl-1 cell monolayers infected with MHV-A59 in  
336 the presence of the PERK inhibitor remarkably showed delayed formation of syncytia in  
337 comparison to untreated cells at 8 h p.i. (Fig 8C), and quantification of released virions through  
338 TCID<sub>50</sub> assays revealed an ~four-fold reduction in virus titre in cells incubated with GSK-260614  
339 compared to control cells ( $P = 0.064$ ; S4B Fig). These observations suggest that relieving inhibition  
340 of protein synthesis – affecting both cellular and viral proteins – is detrimental to virus production  
341 and the development of syncytia in virus infected cells.

342

343

344

345 **Discussion:**

346

347 We have used ribosome profiling and parallel RNASeq to investigate changes in the cellular  
348 translatome and transcriptome in response to infection with MHV, a representative of the  
349 *Betacoronavirus* genus of the *Coronaviridae* family. These studies provide the highest resolution  
350 data to date on the translatome of cells during coronavirus-induced stress.

351

352 RNASeq libraries revealed that some of the most significantly upregulated cellular transcripts in  
353 virus-infected cells were part of the UPR (*Herpud1* and *Chac1*) and changes in the translation  
354 efficiency of cellular proteins were consistent with uORF-regulated responses to eIF2 $\alpha$   
355 phosphorylation, including those previously implicated as effectors of the UPR such as in *Atf4*, *Atf5*  
356 and *Chop* [34-39]. These high-resolution data confirm again that there is a close interplay between  
357 virus infection and the UPR, with the host activating the UPR to combat the effects of virus  
358 infection, and viruses sometimes manipulating the UPR to promote replication and pathogenesis  
359 [56-59]. The intimate association of CoVs with the ER during replication results in ER stress  
360 responses as the cell attempts to return to homeostasis [46, 60-64; reviewed in [65]).

361

362 The relative modulation of UPR branches differs between different CoVs [3,5,65]. For example,  
363 SARS-CoV infection does not lead to *Xbp-1* splicing [46] whereas the IRE1 pathway is activated by  
364 infectious bronchitis virus or MHV infection or by MHV S protein overexpression [29,66]. In spite  
365 of the observed *Xbp-1* mRNA splicing during MHV infection [29], Xbp-1s protein had not  
366 previously been detected in coronavirus-infected cells. In our study (8 h p.i. data set), an increased  
367 number of RPF reads mapped in the +2 reading frame of the *Xbp-1u* transcript corresponding to  
368 translation of the *Xbp-1s* frameshifted isoform.

369

370 Activation of the ATF6 pathway by CoV infection has not yet been fully addressed. ATF6 cleavage  
371 into its active form is observed during MHV infection but is significantly reduced at late time points  
372 [29]. On the other hand, the trimmed ATF6 form is not detected in SARS-CoV infected cells [67].  
373 Furthermore, ER stress-responsive promoters exhibit little activity under these conditions. In the  
374 present study, an induction of *BiP/Grp78* transcription due to ATF6 activation was observed to a  
375 similar extent in both tunicamycin-treated and MHV-infected cells, whereas BiP/Grp78 protein  
376 expression was only detected by western blotting in tunicamycin-treated cells. Ribosome profiling  
377 data revealed that, in virus-infected cells, the amount of RPFs corresponding to the *BiP* CDS was  
378 not as high as in tunicamycin-treated cells and this was probably the reason why this protein was  
379 not detected by western blot analysis.

380

381 With respect to the UPR-related inhibition mediated by eIF2 $\alpha$  phosphorylation, it has been shown  
382 that infectious bronchitis virus activates or suppresses protein kinase RNA-activated (PKR) and  
383 PERK during the course of an infection [68] whereas transmissible gastroenteritis virus protein 7  
384 emulates the function of DNA damage-inducible protein 34 (GADD34) to dephosphorylate eIF2 $\alpha$   
385 [69]. Our study has now shown that MHV-A59 infection increases the level of p-eIF2 $\alpha$  and ATF4  
386 from 5 h p.i. onwards. The RiboSeq data also revealed decreased translation of the *Atf4* uORF2 at 8  
387 h p.i. and a concomitant increase in translation of the main ORF. Although [29] failed to detect the  
388 products of ATF4 target genes, *Gadd34* and *Chop*, during MHV infection by western blotting, we  
389 found evidence supporting an increase in transcription and translation of *Chop* at later time points  
390 p.i.

391

392 We tested the effect of the selective PERK inhibitor GSK-260614 on MHV replication [54,55].  
393 GSK-260614 ( $IC_{50} = 0.4$  nM) exhibits >1000-fold selectivity for PERK over heme-regulated eIF2 $\alpha$   
394 (HR1) and PKR. Up to 5  $\mu$ M of this inhibitor was well tolerated by 17 Cl-1 cells and, in MHV-  
395 infected cells, the prevention of eIF2 $\alpha$  phosphorylation alleviated the inhibition in translation of

396 cellular and viral proteins as expected. Surprisingly, the higher content of viral proteins did not lead  
397 to a more prominent cytopathic effect but instead delayed syncytia formation and reduced viral titre.  
398 Therefore, we conclude that UPR-mediated eIF2 $\alpha$  phosphorylation may be favourable to MHV  
399 replication – perhaps by preventing translation of various anti-viral factors – and the  
400 pharmacological manipulation of this UPR branch can be explored as a potential target for antiviral  
401 intervention.

402

403 Our previous analysis of RPFs mapping to host mRNAs during MHV infection [16] indicated a  
404 remarkable perturbation in ribosome distributions at late time points, with a greatly increased  
405 proportion of RPFs mapping to the first ~30–40 codons of coding regions. In yeast, it has been  
406 reported that an accumulation of reads in the 5' region of coding sequences specifically under cell  
407 stress is an artefact of cycloheximide pretreatment, and it has been hypothesized that stressed cells  
408 might have a slower rate of cycloheximide uptake leading to increased mean post-initiation  
409 ribosome run-on times prior to cycloheximide-induced arrest of elongation [43,44]. Thus, it was  
410 unclear whether this artefact might also occur in mammalian cells given that mammalian cells lack  
411 a cell wall. Our results show that this artefact does indeed extend to mammalian cells and thus call  
412 into question the interpretations put forward by [41] and [42] for the similar perturbations in  
413 ribosome density observed when cells were subjected to heat shock or proteotoxic stress. Further,  
414 we find that the magnitude of this artefact depends on the type of stress and, in the case of MHV  
415 infection, is not alleviated by increasing the concentration of cycloheximide to 100 times the  
416 standard amount, but can be alleviated completely by flash freezing without cycloheximide  
417 pretreatment. Since the artefact also occurs in mammalian cells, it is possible that it is not related  
418 simply to cycloheximide uptake rates. Potentially it may instead be related to dysregulation of the  
419 translational machinery under stress in a way that reduces cycloheximide efficiency (e.g. due to  
420 alterations in ribosomal exit (E)-site tRNA occupancy).

421

422 Ribosome profiling provides information on initiating and elongating 80S ribosomes but it does not  
423 account for free monosomes or early stages in initiation prior to formation of the 80S complex.  
424 Analytical polysome profiling showed an accumulation of 80S monosomes in MHV-infected cells  
425 from 5 h p.i. with the vast majority not being associated with mRNA which is a typical outcome of  
426 impaired translation [70]. This suggests that protein translation was inhibited at the stage of  
427 initiation probably due to the activation of the PERK branch in response to ER stress and the  
428 concomitant phosphorylation of eIF2 $\alpha$ . Phosphorylated eIF2 $\alpha$  (p-eIF2 $\alpha$ ) forms a stable complex  
429 with eIF2B – the guanine exchange factor responsible for recycling inactive eIF2-GDP to eIF2-GTP  
430 – which rapidly reduces the pool of available eIF2B. This prevents recycling of the ternary complex  
431 of eIF2, GTP and Met-tRNAi and formation of the 43S pre-initiation complex, and thus leads to a  
432 general shutdown of protein synthesis by inhibition of initiation [71].

433

434 Viruses commonly employ translational shutoff mechanisms to facilitate viral replication. On the  
435 one hand, shut-off of host cell translation can redirect the translation machinery towards viral gene  
436 expression if the virus has evolved non-canonical modes of translation, such as internal ribosome  
437 entry site (IRES) mediated initiation. On the other hand, the shut-off of host cell protein synthesis  
438 will inhibit a range of cellular anti-viral responses. Previous studies have shown that MHV can  
439 induce host translational shutoff and mRNA decay in LR7 cells with the concomitant formation of  
440 stress granules and processing bodies [28]. Furthermore, a number of reports have demonstrated  
441 that CoV nsp1, the most N-terminal product of the replicase polyprotein, modulates host protein  
442 synthesis. In different CoVs, nsp1 has been shown to associate with the 40S ribosomal subunit thus  
443 preventing viral and cellular mRNA translation; induce cellular mRNA degradation via an  
444 endonucleolytic mRNA cleavage in the 5' region of capped mRNA; and selectively target nuclear  
445 host mRNAs and transport them to the cytoplasm for degradation [30-31,72-73]. The involvement  
446 of nsp1 in host protein translation could not be ruled out in this study without a comparison with a  
447 mutant virus lacking nsp1. However, the UPR-related translational modulation and the CoV nsp1-

448 related modification of translation (and mRNA degradation) testify to the complexity of cellular  
449 translational shutoff mechanisms utilized by CoVs. How MHV proteins can be synthesized in a  
450 state of global translation inhibition has been the subject of previous speculation. Viral mRNAs  
451 contain a common 5'-leader sequence (65–90 nucleotides long) that could bind to the nucleocapsid  
452 (N) protein to form a complex that might act as a strong translation initiation signal [74], or the  
453 leader RNA sequence may bind to nsp1, protecting the viral mRNAs from nsp1-induced RNA  
454 cleavage [73,75]. However, we found previously that virus mRNAs 2–7 were translated with  
455 generally similar efficiencies during infection and, importantly, were not preferentially translated  
456 relative to host mRNAs. Thus we concluded that the synthesis of large quantities of virus proteins,  
457 especially N, was achieved mainly through high levels of transcription [16].

458

459 In conclusion, this study provides a survey of coronavirus effects on the cellular transcriptome and  
460 translatome, complementing previous investigations on the UPR and host cell shutoff during MHV  
461 infection. The results of our analyses will help inform further investigations on host-CoV  
462 interactions and may help identify new targets for antiviral intervention.

463

#### 464 Materials and Methods:

465

466 **Ribosomal profiling and RNASeq data:** Virus sequencing data (RNASeq and RiboSeq with  
467 cycloheximide pretreatment) were generated previously [16] and have been deposited in the  
468 ArrayExpress database (<http://www.ebi.ac.uk/arrayexpress>) under the accession number E-MTAB-  
469 4111.

470 Data for the tunicamycin and flash freezing sequencing experiments have been deposited in  
471 ArrayExpress under the accession numbers E-MTAB-5391 and E-MTAB-6278 respectively.

472

473 For the tunicamycin experiments, 17 Cl-1 cells were incubated in the presence of tunicamycin (2  
474 µg/ml) and, after 6 h, cells were treated with CHX (Sigma-Aldrich; to 100 µg/ml or 10 mg/ml; 2  
475 min). Cells were rinsed with 5 ml of ice-cold PBS and then submerged in a reservoir of liquid  
476 nitrogen for 10 s. For flash freezing experiments, cells were rinsed with 5 ml of ice-cold PBS and  
477 then submerged in liquid nitrogen for 10 s. Cell lysates were subjected to RiboSeq and RNASeq as  
478 previously described [16,76].

479

480 **Computational analysis of RiboSeq and RNASeq data:** Reads were trimmed for adaptor  
481 sequences, filtered for length  $\geq$  25 nt, and reads mapping to *Mus musculus* rRNA (with up to 2  
482 mismatches) removed, as previously described [16]. The remaining reads were aligned directly to  
483 the mouse genome (UCSC, assembly mm10) (with up to 2 mismatches) using TopHat (parameters:  
484 --no-novel-juncs --bowtie1 --prefilter-multihits --max-multihits 500, with --transcriptome-index  
485 defined using the genes.gtf file from the UCSC mm10 annotation available from the TopHat  
486 website) [77]. Reads were tabulated using htseq-count (parameters: -t CDS -m intersection-strict -i  
487 gene\_id -s yes), using the NCBI RefSeq mRNAs as the gene feature annotation. For differential  
488 expression analyses, the htseq-count parameter “-type CDS” was used to count only those reads  
489 (both RiboSeq and RNASeq) that mapped to the annotated coding regions of transcripts [78]. Thus  
490 the differential expression analyses exclude reads mapping to uORFs or non-annotated coding  
491 sequences (unless such sequences overlap the main annotated ORF).

492

493 Differential expression analyses on RNASeq or RiboSeq count data were performed with DESeq  
494 [20], EdgeR [21], NOISeq [22] and BaySeq [23]. Read counts were normalized by library size prior  
495 to comparison and low count genes (genes with fewer than 1 count per million reads mapping to the  
496 CDS in either the infected or mock libraries) were discarded. For BaySeq analyses, the sample size  
497 used to calculate priors was set to 200000. For each comparison, two replicates from infected cells  
498 at a specific timepoint were compared to four libraries from uninfected cells (two each at 1 and 8 h).

499 Changes in translation efficiency (TE) were estimated using Bayseq in the paired library mode,  
500 Babel [32] and Xtail [33]. A given gene was considered to be differentially expressed if the FDR  
501 was less than 0.05 and the fold change between the averages of infected and mock replicates was  
502 greater than two. Volcano plots and inter-replicate consistency plots were generated using standard  
503 R plotting features and FDR and log<sub>2</sub>(fold change) values from the BaySeq, Babel and Xtail  
504 analyses.

505

506 As reads were mapped to the genome, genomic read mapping locations had to be converted to  
507 transcript-specific coordinates to generate RNASeq and RPF profiles for specific transcripts. Tophat  
508 bam files were sorted by genomic coordinate and indexed using SAMTools [79]. A custom R script  
509 using Rsamtools [80] was developed to extract reads at a given series of genomic loci from the bam  
510 file (corresponding to the exon sequences of a given transcript isoform), convert the genomic  
511 positions of reads to positions relative to the transcript sequence, calculate the phasing of the reads,  
512 and generate plots showing the distribution of reads on the transcript. In some cases it is not  
513 possible to definitively distinguish usage of alternative exons or changes in transcription start sites  
514 or initiation codon utilization. The advantage of the aforementioned visualization process is that it  
515 retains all reads mapping to a given exon allowing for easy manual inspection of data which may  
516 originate from different isoforms. In individual gene plots, read positions for RPFs were offset +12  
517 nt to map the approximate P-site.

518

519 Histograms of 5' end positions of host mRNA reads relative to initiation and termination codons  
520 were derived from reads mapping to RefSeq mRNAs with annotated CDSs  $\geq$ 450 nt in length and  
521 with annotated 5' and 3' UTRs  $\geq$ 60 nt in length. All figures are based on total numbers of mapped  
522 reads, rather than weighted sums for highly expressed mRNAs.

523

524 Ribosome accumulation at the 5' end of coding sequences was assessed via a 5' loading ratio  
525 statistic. Specifically, the density of RPFs with estimated P-sites mapping within nucleotide  
526 positions 16–90 of a given ORF was compared with the density of reads in the downstream portion  
527 of the ORF (ending 15 nt before the ORF stop codon). These windows were designed to exclude the  
528 accumulation of ribosomes involved in initiation and termination. We then compared the loading  
529 ratio in infected samples with the loading ratio in mocks for each gene.

530

531 **Cells and virus:** Murine 17 clone 1 (17 Cl-1) ([81], a kind gift of Dr Stanley Sawicki, University of  
532 Toledo) cells were maintained in Dulbecco's modification of Eagle's medium supplemented with  
533 10% (vol/vol) fetal calf serum (FCS). Recombinant MHV strain A59 (MHV-A59) was derived as  
534 previously described ([82], a kind gift of Dr Stanley Sawicki, University of Toledo, ATCC VR764).  
535 Upon reaching 70–80% confluence, 17 Cl-1 cells were infected with MHV-A59 at MOI 10 in  
536 infection medium [Hank's balanced salt solution (HBSS) containing 50 µg/ml DEAE-dextran and  
537 0.2% bovine serum albumin (BSA)]. After 45 min at 37 °C, the inoculum was removed and the cells  
538 were incubated in DMEM containing 10% FCS, 100 U/ml penicillin and 100 µg/ml streptomycin at  
539 37 °C until harvest.

540 17 Cl-1 mock and MHV-infected cells were treated with different concentrations (1–5 µM) of the  
541 PERK-inhibitor GSK-2606414, a kind gift of Dr Edward Emmott and Prof Ian Goodfellow. GSK-  
542 2606414 was added to the cells just after the adsorption time and maintained until cells were  
543 harvested.

544

545 **Quantitative real-time PCR assays:** Total RNA was isolated as described previously [76] for  
546 RNA-Seq analysis, and cDNA was synthesized from 1 µg total RNA. Transcript levels were  
547 determined by quantitative real-time PCR using a Rotor-Gene 3000 (Corbett Research). Reactions  
548 were performed in a final volume of 20 µl containing Hot Start Taq (1 U; QIAGEN), 3.5 mM  
549 MgCl<sub>2</sub>, 2.5 mM deoxynucleotides, SYBR Green dye, 500 nM forward and reverse specific primers

550 and 1 µl of cDNA. After enzyme activation (95 °C, 15 min), amplification was carried out in a  
551 three-step PCR procedure (50 cycles: 15 s at 95 °C for denaturation, 20 s at 55 °C for annealing and  
552 20 s at 72 °C for extension). Non-template controls were included for each primer pair, and each  
553 PCR reaction was carried out in triplicate.

554

555 **Immunoblotting:** Proteins were separated by 10% or 12% SDS-PAGE and transferred to  
556 nitrocellulose membranes. These were blocked (5% non-fat milk powder in PBST [137 mM NaCl,  
557 2.7 mM KCl, 10 mM Na<sub>2</sub>HPO<sub>4</sub>, 1.5 mM KH<sub>2</sub>PO<sub>4</sub>, pH 6.7, and 0.1% Tween 20]) and probed with  
558 mouse monoclonal antibodies raised against N (1:1,000), S (1:500) - kind gifts of Dr Helmut Wege,  
559 University of Würzburg -, GAPDH (G8795, Sigma-Aldrich, 1:20,000), S6 (1:500, Cell Signaling);  
560 rabbit monoclonal antibodies against Grp78/BiP (1:1,000, Abcam) and RPL10a (1:500, Abcam); or  
561 polyclonal rabbit anti-ATF4 (1:500, Proteintech), anti-eIF2α and anti-p(Ser-51)-eIF2α (1:1,000,  
562 Cell Signaling). Membranes were incubated in the dark with an IRDye-conjugated secondary  
563 antibody in phosphate-buffered saline (PBS) and 0.1% Tween 20 [IRDye 800CW Donkey Anti-  
564 Mouse IgG (H+L), IRDye 800CW Donkey Anti-Rabbit IgG (H+L), IRDye 680RD Goat Anti-  
565 Mouse IgG (H+L) and IRDye 680RD Goat Anti-Mouse IgM (µ chain specific)]. Blots were  
566 scanned using an Odyssey Infrared Imaging System (Licor).

567

568 **Polysome profiling:** 17 Cl-1 cells were infected as previously described. Ten minutes prior to  
569 harvesting, cells were treated with cycloheximide (100 µg/ml), washed with PBS and lysed in a  
570 buffer containing 20 mM Tris HCl pH 7.5, 100 mM KCl, 5 mM MgOAc, 0.375 mM CHX, 1 mM  
571 DTT, 0.1 mM PMSF, 2U/µl DNase I, 0.5% NP-40, supplemented with protease and phosphatase  
572 inhibitors (ThermoFisher Scientific). Following trituration with a 26-G needle (ten passes), lysates  
573 were cleared (13,000 g at 4 °C for 20 min) and the supernatants layered onto 12 mL sucrose density  
574 gradients (10–50% sucrose in TMK buffer – 20 mM Tris-HCl pH 7.5, 100 mM KCl, 5 mM MgCl<sub>2</sub>)  
575 prepared in Beckman SW41 polypropylene tubes using a Gradient Master (Biocomp). Following

576 centrifugation (200,000 g for 90 min at 4 °C), fractions were prepared using an ISCO fractionator  
577 monitoring absorbance at 254 nm. Proteins were concentrated from fractions using methanol-  
578 chloroform extraction [83] and subjected to immunoblotting analysis. Polysome profiling in higher  
579 salt conditions was carried out as described above except that the lysis buffer and sucrose density  
580 gradient contained 400 mM KCl.

581

582 **Metabolic labelling:** 17 Cl-1 cell monolayers were infected with MHV A-59 at a MOI of 10  
583 PFU/cell. At 5 h p.i., cells were washed twice with PBS and labelled for 1 h in methionine-free  
584 DMEM supplemented with 125 µCi/ml [<sup>35</sup>S] methionine. After this period, cells were harvested,  
585 washed twice with PBS and resuspended in lysis buffer (50 mM Tris pH 7.5, 100 mM NaCl, 5 mM  
586 EDTA, 0.5% NP40). Cell lysate aliquots were mixed with Laemmli's sample buffer to a final  
587 concentration of 1× and subjected to 10% SDS-PAGE followed by autoradiography.

588

589 **References:**

- 590 1. Channappanavar R, Perlman S (2017) Pathogenic human coronavirus infections: causes and  
591 consequences of cytokine storm and immunopathology. *Semin Immunopathol.* doi:  
592 10.1007/s00281-017-0629-x.
- 593 2. Walsh D, Mathews MB, Mohr I (2013) Tinkering with translation: protein synthesis in virus-  
595 infected cells. *Cold Spring Harb Perspect Biol* 5:a012351.
- 596 3. Fung TS, Liu DX (2014) Coronavirus infection, ER stress, apoptosis and innate immunity. *Front  
598 Microbiol* 5: 296.
- 599 4. Ron D, Walter P (2007) Signal integration in the endoplasmic reticulum unfolded protein  
601 response. *Nat Rev Mol Cell Biol* 8: 519-529.
- 602 5. Fung TS, Liao Y, Liu DX (2016) Regulation of stress responses and translational control by  
604 coronavirus. *Viruses* 8: E184.
- 605 6. Ingolia NT, Ghaemmaghami S, Newman JR, Weissman JS (2009) Genome-wide analysis in vivo  
607 of translation with nucleotide resolution using ribosome profiling. *Science* 324: 218-223.
- 608 7. Ingolia NT, Lareau LF, Weissman JS (2011) Ribosome profiling of mouse embryonic stem cells  
610 reveals the complexity and dynamics of mammalian proteomes. *Cell* 147: 789-802.
- 611 8. Ingolia NT (2014) Ribosome profiling: new views of translation, from single codons to genome  
613 scale. *Nat Rev Genet* 15: 205-213.

614

- 615 9. Stern-Ginossar N, Weisburd B, Michalski A, Le VT, Hein MY, Huang SX, Ma M, Shen B, Qian  
616 SB, Hengel H, et al (2012) Decoding human cytomegalovirus. *Science* 338: 1088-1093.  
617
- 618 10. Liu X, Jiang H, Gu Z, Roberts, JW (2013) High-resolution view of bacteriophage lambda gene  
619 expression by ribosome profiling. *Proc Natl Acad Sci U S A* 110: 11928-11933.  
620
- 621 11. Arias C, Weisburd B, Stern-Ginossar N, Mercier A, Madrid AS, Bellare P, Holdorf M,  
622 Weissman JS, Ganem D (2014) KSHV 2.0: a comprehensive annotation of the Kaposi's sarcoma-  
623 associated herpesvirus genome using next-generation sequencing reveals novel genomic and  
624 functional features. *PLoS Pathog* 10: e1003847.  
625
- 626 12. Rutkowski AJ, Erhard F, L'Hernault A, Bonfert T, Schilhabel M, Crump C, Rosenstiel P,  
627 Efsthathiou S, Zimmer R, Friedel CC, et al (2015) Widespread disruption of host transcription  
628 termination in HSV-1 infection. *Nat Commun* 6: 7126.  
629
- 630 13. Tirosh O, Cohen Y, Shitrit A, Shani O, Le-Trilling VT, Trilling M, Friedlander G, Tanenbaum  
631 M, Stern-Ginossar N (2015) The transcription and translation landscapes during human  
632 cytomegalovirus infection reveal novel host-pathogen interactions. *PLoS Pathog* 11: e1005288.  
633
- 634 14. Yang Z, Cao S, Martens CA, Porcella SF, Xie Z, Ma M, Shen B, Moss B (2015) Deciphering  
635 poxvirus gene expression by RNA sequencing and ribosome profiling. *J Virol* 89: 6874-6886.  
636
- 637 15. Bercovich-Kinori A, Tai J, Gelbart IA, Shitrit A, Ben-Moshe S, Drori Y, Itzkovitz S,  
638 Mandelboim M, Stern-Ginossar N (2016) A systematic view on influenza induced host shutoff.  
639 *Elife* 5: e18311.  
640
- 641 16. Irigoyen N, Firth AE, Jones JD, Chung BY, Siddell SG, Brierley I (2016) High-resolution  
642 analysis of coronavirus gene expression by RNA sequencing and ribosome profiling. *PLoS Pathog*  
643 12: e1005473.  
644
- 645 17. Dai A, Cao S, Dhungel P, Luan Y, Liu Y, Xie Z, Yang Z (2017) Ribosome profiling reveals  
646 translational upregulation of cellular oxidative phosphorylation mRNAs during vaccinia virus-  
647 induced host shutoff. *J Virol* 91: e01858.16.  
648
- 649 18. Irigoyen N, Dinan AM, Brierley I, Firth AE (2018) Ribosome profiling of the retrovirus murine  
650 leukemia virus. *Retrovirology* 15: 10.  
651
- 652 19. Reid DW, Campos RK, Child JR, Zheng T, Chan KWK, Bradrick SS, Vasudevan SG, Garcia-  
653 Blanco MA, Nicchitta CV (2018) Dengue virus selectively annexes endoplasmic reticulum-  
654 associated translation machinery as a strategy for co-opting host cell protein synthesis. *J Virol*  
655 92:e01766-17.  
656
- 657 20. Anders S, Reyes A, Huber W (2012) Detecting differential usage of exons from RNA-seq data.  
658 *Genome Res* 22: 2008-2017.  
659
- 660 21. Robinson MD, McCarthy DJ, Smyth GK (2010) edgeR: a Bioconductor package for differential  
661 expression analysis of digital gene expression data. *Bioinformatics* 26: 130-140.  
662
- 663 22. Tarazona S, Furió-Tarí P, Turrà D, Pietro AD, Nueda MJ, Ferrer A, Conesa A (2015) Data  
664 quality aware analysis of differential expression in RNA-seq with NOISeq R/Bioc package. *Nucleic  
665 Acids Res* 43: e140.  
666

- 667 23. Hardcastle TJ, Kelly KA (2010) baySeq: empirical Bayesian methods for identifying differential  
668 expression in sequence count data. BMC Bioinformatics 11: 422.  
669  
670 24. Hollien J, Weissman JS (2006) Decay of endoplasmic reticulum-localized mRNAs during the  
671 unfolded protein response. Science 313: 104-107.  
672  
673 25. Hiramatsu N, Joseph VT, Lin JH (2011) Monitoring and manipulating mammalian unfolded  
674 protein response. Methods Enzymol 491: 183-198.  
675  
676 26. Siddell SG, Wege H, Barthel, A, ter Meulen V (1980) Coronavirus JHM: cell-free synthesis of  
677 structural protein p60. J Virol 33: 10-17.  
678  
679 27. Hilton A, Mizzen L, MacIntyre G, Cheley S, Anderson R (1986) Translational control in murine  
680 hepatitis virus infection. J Gen Virol 67: 923-932.  
681  
682 28. Raaben M, Groot Koerkamp MJ, Rottier PJ, de Haan CA (2007) Mouse hepatitis coronavirus  
683 replication induces host translational shutoff and mRNA decay, with concomitant formation of  
684 stress granules and processing bodies. Cell Microbiol 9: 2218-2229.  
685  
686 29. Bechill J, Chen Z, Brewer JW, Baker SC (2008) Coronavirus infection modulates the unfolded  
687 protein response and mediates sustained translational repression. J Virol 82: 4492-4501.  
688  
689 30. Kamitani W, Huang C, Narayanan K, Lokugamage KG, Makino S (2009) A two-pronged  
690 strategy to suppress host protein synthesis by SARS coronavirus Nsp1. Nat Struct Mol Biol 16:  
691 1134-1140.  
692  
693 31. Lokugamage KG, Narayanan K, Nakagawa K, Terasaki K, Ramirez SI, Tseng CT, Makino S  
694 (2015) Middle east respiratory syndrome coronavirus nsp1 inhibits host gene expression by  
695 selectively targeting mRNAs transcribed in the nucleus while sparing mRNAs of cytoplasmic  
696 origin. J Virol 89: 10970-10981.  
697  
698 32. Olshen AB, Hsieh AC, Stumpf CR, Olshen RA, Ruggero D, Taylor BS (2013) Assessing gene-  
699 level translational control from ribosome profiling. Bioinformatics 29: 2995-3002.  
700  
701 33. Xiao Z, Zou Q, Liu Y, Yang X (2016) Genome-wide assessment of differential translations with  
702 ribosome profiling data. Nat Commun 7: 11194.  
703  
704 34. Lu PD, Harding HP, Ron D (2004) Translation reinitiation at alternative open reading frames  
705 regulates gene expression in an integrated stress response. J Cell Biol 167: 27-33.  
706  
707 35. Vattem KM, Wek RC (2004) Reinitiation involving upstream ORFs regulates ATF4 mRNA  
708 translation in mammalian cells. Proc Natl Acad Sci U S A 101: 11269-11274.  
709  
710 36. Watatani Y, Ichikawa K, Nakanishi N, Fujimoto M, Takeda H, Kimura N, Hirose H, Takahashi  
711 S, Takahashi Y (2008) Stress-induced translation of ATF5 mRNA is regulated by the 5'-  
712 untranslated region. J Biol Chem 283: 2543-2553.  
713  
714 37. Zhou D, Palam LR, Jiang L, Narasimhan J, Staschke KA, Wek RC (2008) Phosphorylation of  
715 eIF2 directs ATF5 translational control in response to diverse stress conditions. J Biol Chem 283:  
716 7064-7073.  
717

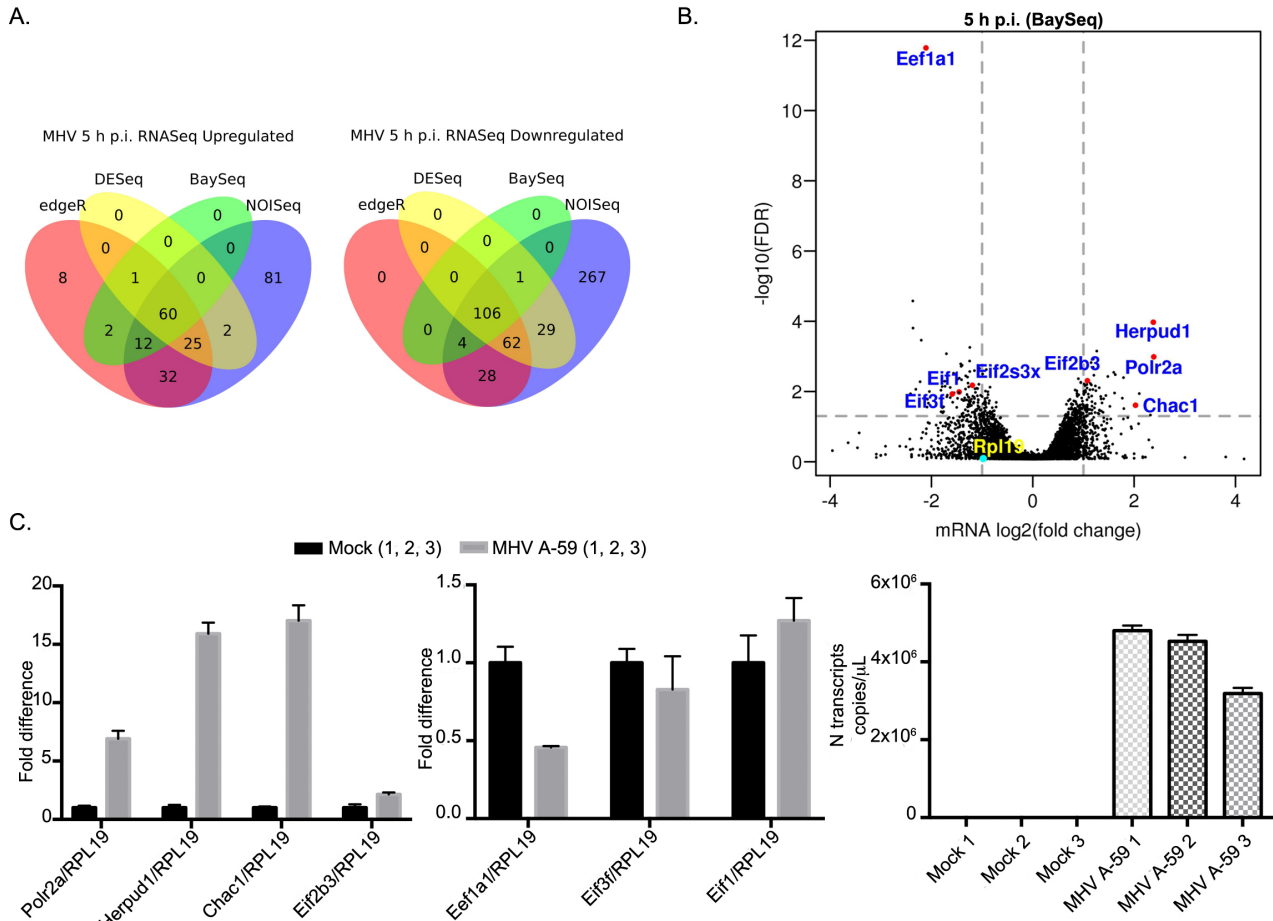
- 718 38. Palam LR, Baird TD, Wek RC (2011) Phosphorylation of eIF2 facilitates ribosomal bypass of  
719 an inhibitory upstream ORF to enhance CHOP translation. *J Biol Chem* 286: 10939-10949.  
720
- 721 39. Andreev DE, O'Connor PB, Fahey C, Kenny EM, Terenin IM, Dmitriev SE, Cormican P,  
722 Morris DW, Shatsky IN, Baranov PV (2015) Translation of 5'leaders is pervasive in genes resistant  
723 to eIF2 repression. *Elife* 4: e03971.  
724
- 725 40. Gerashchenko MV, Lobanov AV, Gladyshev VN (2012) Genome-wide ribosome profiling  
726 reveals complex translational regulation in response to oxidative stress. *Proc Natl Acad Sci U S A*  
727 109: 17394-17399.  
728
- 729 41. Liu B, Han Y, Qian SB (2013) Cotranslational response to proteotoxic stress by elongation  
730 pausing of ribosomes. *Mol Cell* 49: 453-463.  
731
- 732 42. Shalgi R, Hurt JA, Krykbaeva I, Taipale M, Lindquist S, Burge CB (2013) Widespread  
733 regulation of translation by elongation pausing in heat shock. *Mol Cell* 49: 439-452.  
734
- 735 43. Gerashchenko MV, Gladyshev VN (2014) Translation inhibitors cause abnormalities in  
736 ribosome profiling experiments. *Nucleic Acids Res* 42: e134.  
737
- 738 44. Duncan CDS, Mata J (2017) Effects of cycloheximide on the interpretation of ribosome  
739 profiling experiments in *Schizosaccharomyces pombe*. *Sci Rep* 7: 10331.  
740
- 741 45. Jiang XS, Tang LY, Dai J, Zhou H, Li SJ, Xia QC, Wu JR, Zeng R (2005) Quantitative analysis  
742 of severe acute respiratory syndrome (SARS)-associated coronavirus-infected cells using proteomic  
743 approaches: implications for cellular responses to virus infection. *Mol Cell Proteomics* 4: 902-913.  
744
- 745 46. Versteeg GA, van de Nes PS, Bredenbeek PJ, Spaan WJ (2007) The coronavirus spike protein  
746 induces endoplasmic reticulum stress and upregulation of intracellular chemokine mRNA  
747 concentrations. *J Virol* 81: 10981-10990.  
748
- 749 47. Yeung YS, Yip CW, Hon CC, Chow KY, Ma IC, Zeng F, Leung FC (2008) Transcriptional  
750 profiling of Vero E6 cells over-expressing SARS-CoV s2 subunit: insights on viral regulation of  
751 apoptosis and proliferation. *Virology* 371: 32-43.  
752
- 753 48. Ye J, Rawson RB, Komuro R, Chen X, Davé UP, Prywes R, Brown MS, Goldstein JL (2000)  
754 ER stress induces cleavage of membrane-bound ATF6 by the same proteases that process  
755 SREBPs. *Mol Cell* 6: 1355-1364.  
756
- 757 49. Yoshida H, Matsui T, Yamamoto A, Okada T, Mori K (2001) XBP1 mRNA is induced by  
758 ATF6 and spliced by IRE1 in response to ER stress to produce a highly active transcription factor.  
759 *Cell* 28: 881-891.  
760
- 761 50. Calfon M, Zeng H, Urano F, Till JH, Hubbard SR, Harding HP, Clark SG, Ron D (2002) IRE1  
762 couples endoplasmic reticulum load to secretory capacity by processing the XBP-1 mRNA. *Nature*  
763 415: 92-96.  
764
- 765 51. Harding HP, Zhang Y, Ron D (1999) Protein translation and folding are coupled by an  
766 endoplasmic-reticulum-resident kinase. *Nature* 397: 271-274.  
767
- 768 52. Harding HP, Zhang Y, Bertolotti A, Zeng H, Ron D (2000) Perk is essential for translational  
769 regulation and cell survival during the unfolded protein response. *Mol Cell* 5: 897-904.

- 770  
771 53. Harding HP, Novoa I, Zhang Y, Zeng H, Wek R, Schapira M, Ron D (2000) Regulated  
772 translation initiation controls stress-induced gene expression in mammalian cells. Mol Cell 6: 1099-  
773 1108.  
774  
775 54. Axtell JM, Medina JR, Feng Y, Shu A, Romeril SP, Grant SW, Li WH, Heerding DA, Minthorn  
776 E, Mencken T, Atkins C, Liu Q, Rabindran S, Kumar R, Hong X, Goetz A, Stanley T, Taylor JD,  
777 Sigethy SD, Tomberlin GH, Hassell AM, Kahler KM, Shewchuk LM, Gampe RT (2012) Discovery  
778 of 7-methyl-5-(1-{[3-(trifluoromethyl)phenyl]acetyl}-2,3-dihydro-1H-indol-5-yl)-7H-pyrrolo[2,3-  
779 d]pyrimidin-4-amine (GSK2606414), a potent and selective first-in-class inhibitor of protein kinase  
780 R (PKR)-like endoplasmic reticulum kinase (PERK). J Med Chem 55, 7193-7207.  
781  
782 55. Harding HP, Zyryanova AF, Ron D (2012) Uncoupling proteostasis and development in vitro  
783 with a small molecule inhibitor of the pancreatic endoplasmic reticulum kinase, PERK. J Biol Chem  
784 287, 44338-44344.  
785  
786 56. Lazar C, Uta M, Branza-Nichita N (2014) Modulation of the unfolded protein response by the  
787 human hepatitis B virus. Front Microbiol 5: 433.  
788  
789 57. Carpenter JE, Grose C (2014) Varicella-zoster glycoprotein expression differentially induces the  
790 unfolded protein response in infected cells. Front Microbiol 5: 322.  
791  
792 58. Chan SW (2014) The unfolded protein response in virus infections. Front Microbiol 5: 518.  
793  
794 59. Perera N, Miller JL, Zitzmann N (2017) The role of the unfolded protein response in dengue  
795 virus pathogenesis. Cell Microbiol 19: doi: 10.1111/cmi.12734  
796  
797 60. David-Ferreira JF, Manaker RA (1965) An electron microscopy study of the development of a  
798 mouse hepatitis virus in tissue culture cells. J Cell Biol 24: 57-78.  
799  
800 61. Klumperman J, Locker JK, Meijer A, Horzinek MC, Geuze HJ, Rottier PJ (1994) Coronavirus  
801 M proteins accumulate in the Golgi complex beyond the site of virion budding. J Virol 68: 6523-  
802 6534.  
803  
804 62. Stertz S, Reichelt M, Spiegel M, Kuri T, Martínez-Sobrido L, García-Sastre A, Weber F, Kochs  
805 G (2007) The intracellular sites of early replication and budding of SARS-coronavirus. Virology  
806 361: 304-315.  
807  
808 63. Reggiori F, Monastyrska I, Verheij MH, Calì T, Ulasli M, Bianchi S, Bernasconi R, de Haan  
809 CA, Molinari M (2010) Coronaviruses hijack the LC3-I-positive EDEMosomes, ER-derived  
810 vesicles exporting short-lived ERAD regulators, for replication. Cell Host Microbe 7: 500-508.  
811  
812 64. Maier HJ, Hawes PC, Cottam EM, Mantell J, Verkade P, Monaghan P, Wileman T, Britton P  
813 (2013) Infectious bronchitis virus generates spherules from zippered endoplasmic reticulum  
814 membranes. MBio 4: e00801-13.  
815  
816 65. Fung TS, Liao Y, Liu DX (2014) The endoplasmic reticulum stress sensor IREa protects cells  
817 from apoptosis induced by the coronavirus infectious bronchitis virus. J Virol 88: 12752-12764.  
818  
819 66. Fung TS, Huang M, Liu DX (2014) Coronavirus-induced ER stress response and its  
820 involvement in regulation of coronavirus-host interactions. Virus Res 194: 110-123.  
821

- 822 67. DeDiego ML, Nieto-Torres JL, Jiménez-Guardeño JM, Regla-Nava JA, Alvarez E, Oliveros JC,  
823 Zhao J, Fett C, Perlman S, Enjuanes L (2011) Severe acute respiratory syndrome coronavirus  
824 envelope protein regulates cell stress response and apoptosis. PLoS Pathog 7: e1002315.  
825
- 826 68. Liao Y, Fung TS, Huang M, Fang SG, Zhong Y, Liu DX (2013) Upregulation of  
827 CHOP/GADD153 during coronavirus infectious bronchitis virus infection modulates apoptosis by  
828 restricting activation of the extracellular signal-regulated kinase pathway. J Virol 87: 8124-8134.  
829
- 830 69. Cruz JL, Sola I, Becares M, Alberca B, Plana J, Enjuanes L, Zuñiga S (2011) Coronavirus gene  
831 7 counteracts host defenses and modulates virus virulence. PLoS Pathog 7: e1002090.  
832
- 833 70. Brina D, Grosso S, Miluzio A, Biffo S (2011) Translational control by 80S formation and 60S  
834 availability: the central role of eIF6, a rate limiting factor in cell cycle progression and  
835 tumorigenesis. Cell Cycle 10, 3441-3446.  
836
- 837 71. Hinnebusch AG (2014) The scanning mechanism of eukaryotic translation initiation. Annu Rev  
838 Biochem 83, 779-812.  
839
- 840 72. Kamitani W, Narayanan K, Huang C, Lokugamage K, Ikegami T, Ito N, Kubo H, Makino S  
841 (2006) Severe acute respiratory syndrome coronavirus nsp1 protein suppresses host gene expression  
842 by promoting host mRNA degradation. Proc Natl Acad Sci U S A 103: 12885-12890.  
843
- 844 73. Huang C, Lokugamage KG, Rozovics JM, Narayanan K, Semler BL, Makino S (2011) SARS  
845 coronavirus nsp1 protein induces template-dependent endonucleolytic cleavage of mRNAs: viral  
846 mRNAs are resistant to nsp1-induced RNA cleavage. PLoS Pathog 7: e1002433.  
847
- 848 74. Tahara SM, Dietlin TA, Bergmann CC, Nelson GW, Kyuwa S, Anthony RP, Stohlman SA  
849 (1994) Coronavirus translational regulation: leader affects mRNA efficiency. Virology 202: 621-  
850 630.  
851
- 852 75. Tanaka T, Kamitani W, DeDiego ML, Enjuanes L, Matsuura Y (2012) Severe acute respiratory  
853 syndrome coronavirus nsp1 facilitates efficient propagation in cells through a specific translational  
854 shutoff of host mRNA. J Virol 86: 11128-11137.  
855
- 856 76. Chung BY, Hardcastle TJ, Jones JD, Irigoyen N, Firth AE, Baulcombe DC, Brierley I (2015)  
857 The use of duplex-specific nuclease in ribosome profiling and a user-friendly software package for  
858 Ribo-seq data analysis. RNA 21: 1731-1745.  
859
- 860 77. Trapnell C, Pachter L, Salzberg SL (2009) TopHat: discovering splice junctions with RNA-Seq.  
861 Bioinformatics 25: 1105-1111.  
862
- 863 78. Anders S, Pyl PT, Huber W (2015) HTSeq - a Python framework to work with high-throughput  
864 sequencing data. Bioinformatics 31: 166-169.  
865
- 866 79. Li H, Handsaker B, Wysoker A, Fennell T, Ruan J, Homer N, Marth G, Abecasis G, Durbin R;  
867 1000 Genome Project Data Processing Subgroup (2009) The sequence alignment/map format and  
868 SAMtools. Bioinformatics 25: 2078-2079.  
869
- 870 80. Delhomme N, Padoleau I, Furlong EE, Steinmetz LM (2012) easyRNASeq: a bioconductor  
871 package for processing RNA-Seq data. Bioinformatics 28: 2532-2533.  
872

- 873 81. Sturman LS, Takemoto KK (1972) Enhanced growth of a murine coronavirus in transformed  
874 mouse cells. *Infect Immun* 6: 501-507.  
875  
876 82. Coley SE, Lavi E, Sawicki SG, Fu L, Schelle B, Karl, N, Siddell SG, Thiel V (2005)  
877 Recombinant mouse hepatitis virus strain A59 from cloned, full-length cDNA replicates to high  
878 titers in vitro and is fully pathogenic *in vivo*. *J Virol* 79: 3097-3106.  
879  
880 83. Eckert EA (1966) Envelope protein(s) derived from influenza virus. *J Bacteriol* 91: 1907-1910.  
881

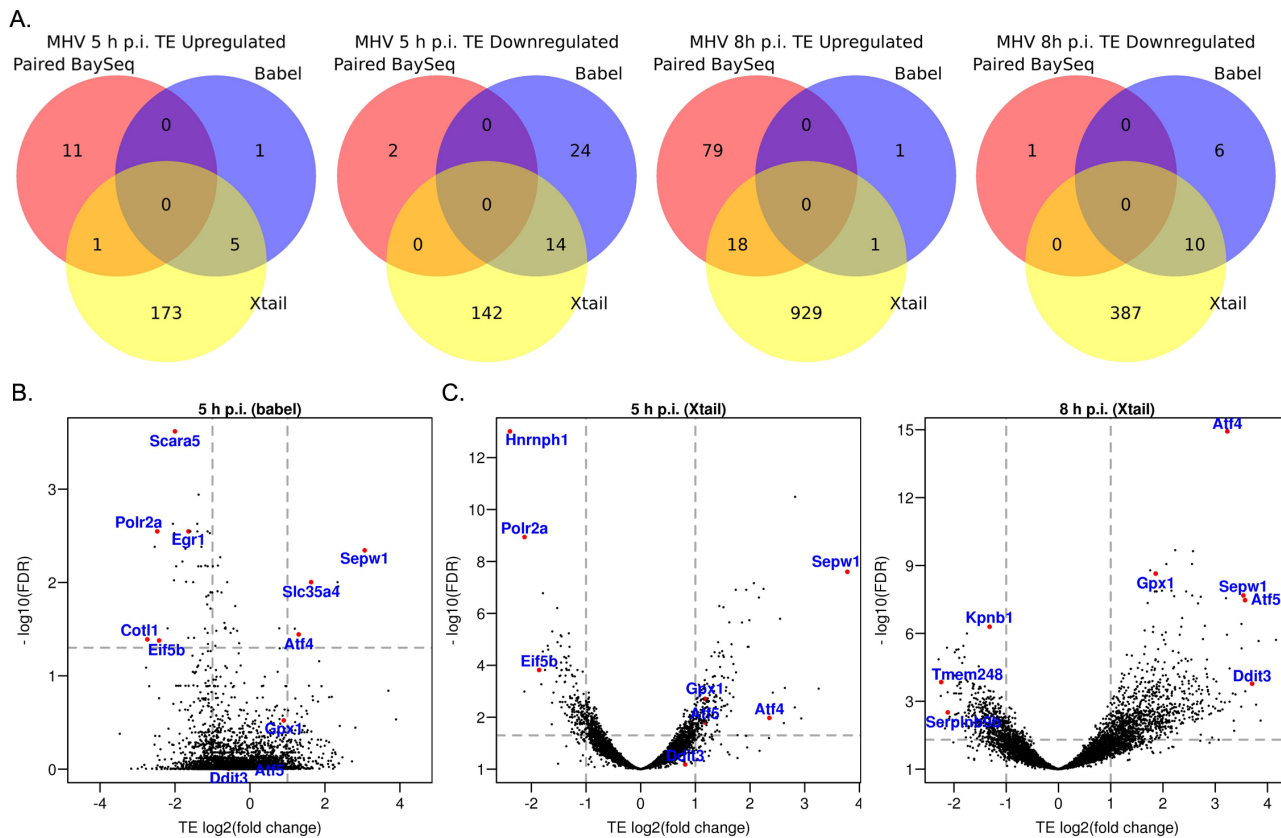
882 **Figure Captions:**



883  
884 **Figure 1: Effect of MHV infection on cellular transcription.** (A) Venn diagrams of upregulated  
885 (left panel) and downregulated (right panel) genes were derived from RNASeq data using four  
886 different methods (edgeR, DESeq, BaySeq and NOISeq). A gene was considered to be  
887 up/downregulated if it had  $\geq 2$  fold change and a FDR  $\leq 0.05$ . Calculations are based on four mock  
888 (two each at 1 and 8 h) and two 5 h p.i. infected samples. (B) Volcano plot showing the relative  
889 change in abundance of cellular genes and the FDR for differential expression using BaySeq. Grey  
890 vertical and horizontal lines indicate a fold change of 2 and a FDR of 0.05, respectively. Selected

891 genes are annotated. **(C)** Quantitative real-time PCR (qRT-PCR) of N transcripts (right panel), and  
892 selected down- (middle panel), and up- (left panel) regulated mRNAs in three biological replicates  
893 of mock- and MHV-infected cells at 5 h p.i. Levels were normalized to ribosomal protein L19  
894 (RPL19) transcript.

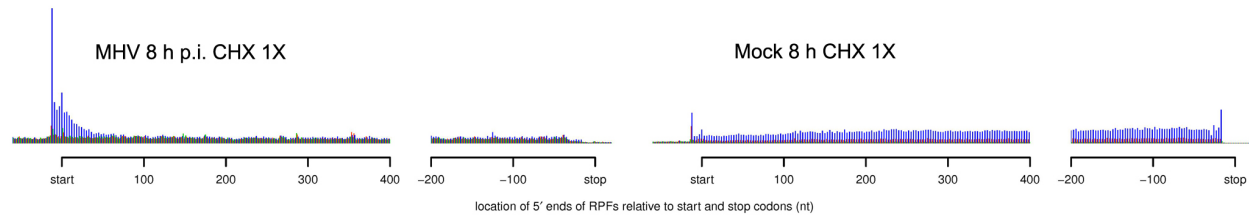
895



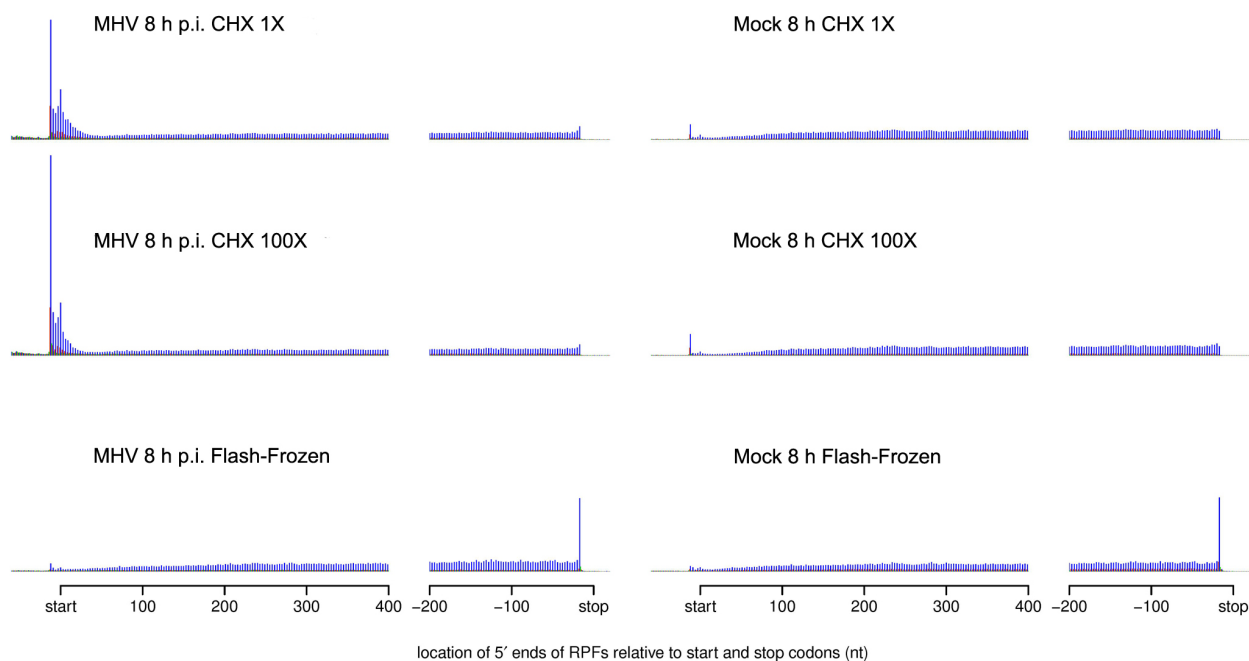
896

897 **Figure 2: Effects of MHV infection on translational efficiency (TE).** **(A)** Venn diagrams of TE  
898 upregulated and downregulated genes using three different methods (Babel, Xtail and paired  
899 BaySeq) at 5 h p.i. (left panels) and 8 h p.i. (right panels). A gene was considered to be  
900 up/downregulated if it had  $\geq 2$  fold change and a FDR  $\leq 0.05$ . Calculations are based on four  
901 RiboSeq/RNASeq pairs of mock (two each at 1 and 8 h) and two RiboSeq/RNASeq pairs of 5 or 8 h  
902 p.i. infected samples. **(B-C)** Volcano plots showing the relative change in TE for cellular genes and  
903 the FDR for differential expression using Babel or Xtail.

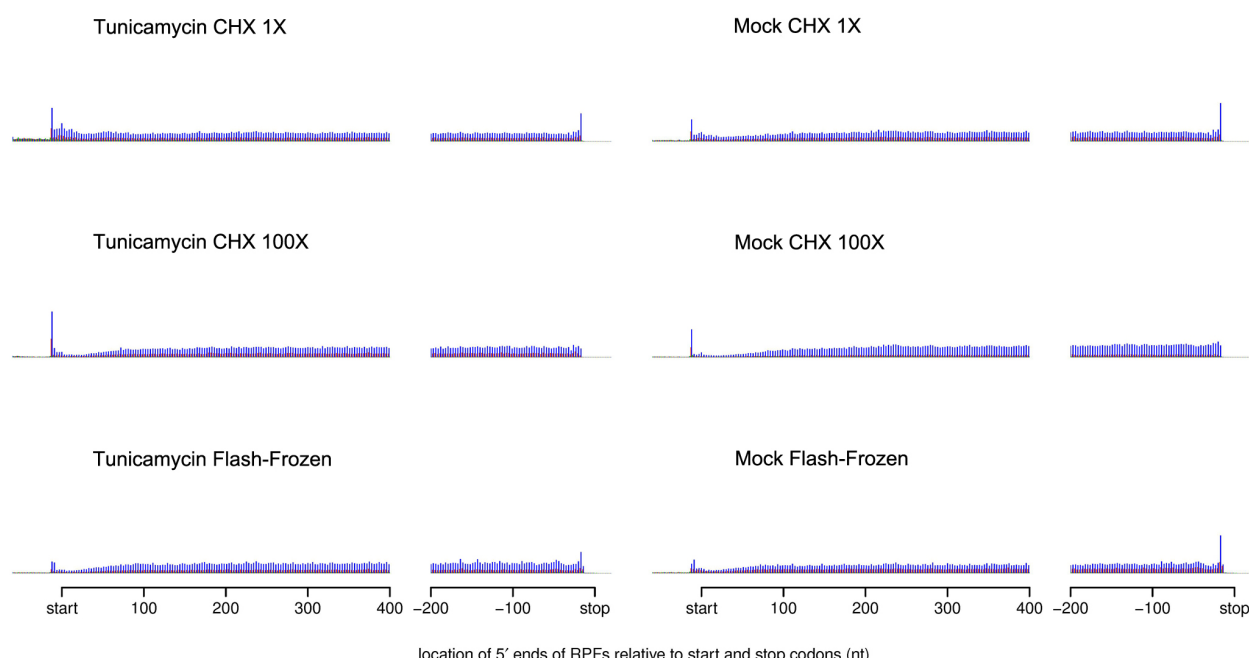
A.



B.



C.



904

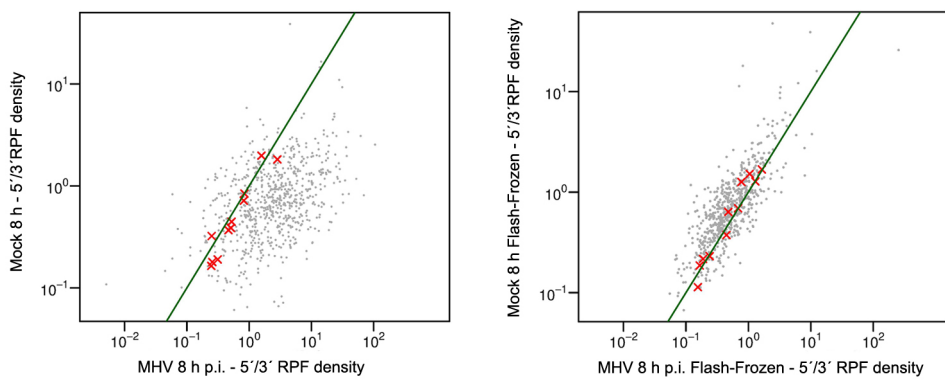
905

906 **Figure 3: Effects of cycloheximide on ribosome profiling of 17 Cl-1 cells infected with MHV-**

**A59. (A)** Mean RPF density on cellular mRNAs (arbitrary y-axis scaling). In the MHV 8 h p.i.

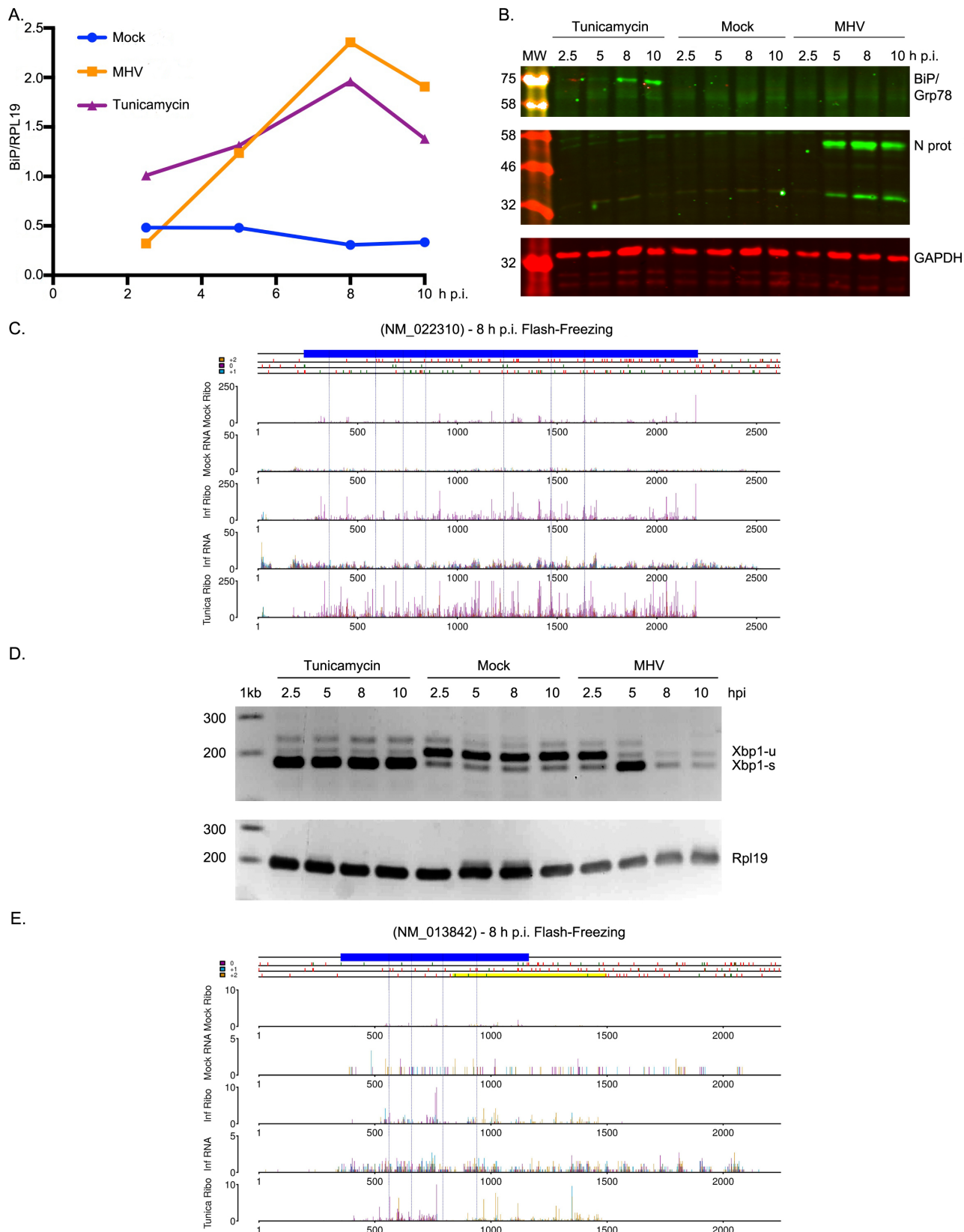
907 RiboSeq library, an increased proportion of reads map to the first ~30–40 codons of CDSs (data  
908 from [16]). **(B)** Meta-analysis of RPFs mapping to cellular mRNAs of 17 Cl-1 cells (right panels)  
909 and 8 h p.i. MHV-infected 17 Cl-1 cells (left panels), harvested with 100 µg/ml cycloheximide  
910 (CHX 1X) or 10 mg/ml cycloheximide (CHX 100X) in the media or harvested by flash freezing in  
911 the absence of cycloheximide. **(C)** Meta-analysis of RPFs mapping to cellular mRNAs of 17 Cl-1  
912 cells (right panels) and 17 Cl-1 cells treated with tunicamycin (2 µg/ml final concentration for 6 h)  
913 (left panels), harvested with 100 µg/ml cycloheximide (CHX 1X) or 10 mg/ml cycloheximide  
914 (CHX 100X) in the media or harvested by flash freezing in the absence of cycloheximide.

915



916

917 **Figure 4: Quantification of ribosome accumulation via a 5' loading ratio statistic.** Scatterplot  
918 comparing the relative density of RPFs in the 5' and 3' portions of cellular mRNA CDSs between  
919 mock and 8 h p.i. infected samples harvested with 100 µg/ml cycloheximide (left panel) or by flash  
920 freezing (right panel). Only genes with ≥50 RPFs mapping between CDS positions 16 and 90 nt in  
921 the 8 h mock are shown. Points below the green diagonal line indicate mRNA species with  
922 increased ribosome density in the 5' regions of coding sequences in infected cells compared to  
923 mock. Red crosses represent mitochondrial CDSs.



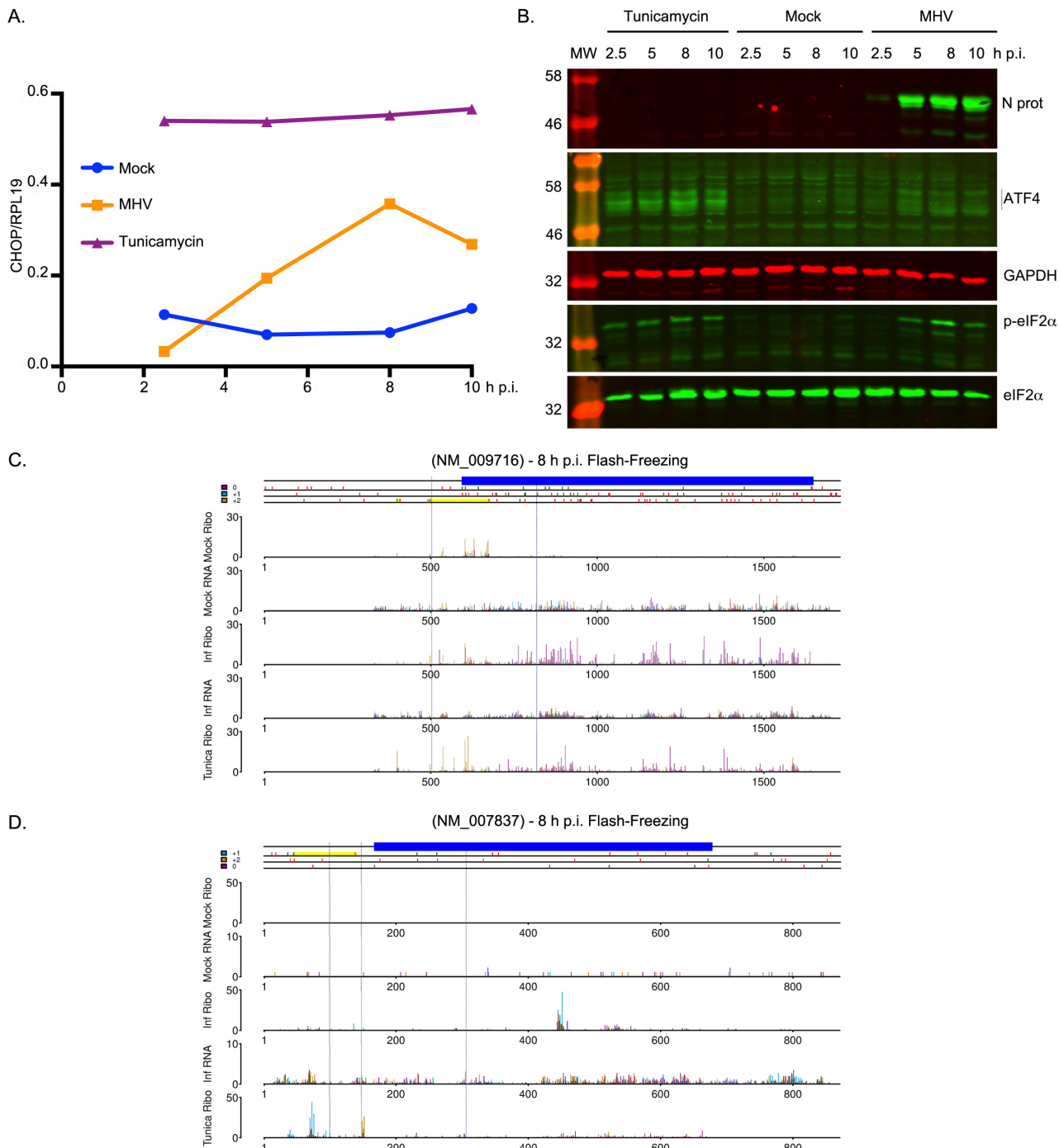
924

925 **Figure 5: Effect of MHV infection on unfolded protein response ATF6 and IRE 1 $\alpha$  activity.** 17

926 Cl-1 cells were incubated in the presence of tunicamycin (2  $\mu$ g/ml) or infected with MHV-A59

927 (MOI 10) and harvested at 2.5, 5, 8 and 10 h.p.i. (A) qRT-PCR of BiP/Grp78 transcripts normalized

928 by *Rpl19* transcript. **(B)** Cell lysates were analysed by 12% SDS-PAGE and immunoblotted using  
929 anti-BiP/Grp78 and anti-N antibodies (green fluorescent secondary antibody). GAPDH was used as  
930 a loading control (red fluorescent secondary antibody). Molecular masses (kDa) are indicated on the  
931 left. **(C)** Analysis of RPFs (Mock Ribo, Inf Ribo and Tunica Ribo) and RNASeq (Mock RNA and  
932 Inf RNA) mapping to *BiP/Grp78*, also known as *Hspa5* (NCBI RefSeq mRNA NM\_022310)  
933 showing, from top to bottom, mock 8 h (Mock), MHV 8 h p.i. (Inf) and tunicamycin treated  
934 (Tunica) cells harvested by flash-freezing. Reads whose 5' end maps to the first, second or third  
935 positions of codons relative to the annotated CDS (blue rectangle) are indicated in purple, blue or  
936 orange, respectively. Green and red tick marks correspond to AUG and stop codons, respectively.  
937 Blue dotted vertical lines indicate annotated exon boundaries. The y-axis shows reads per million  
938 mapped to host mRNAs. Note that in order to properly visualize RPFs across the *BiP/Grp78* ORF,  
939 the y-axis has been truncated leaving some RPF counts for tunicamycin-treated cells off scale. S3  
940 Fig shows the non-modified gene-plot for *BiP/Grp78*. **(D)** RT-PCR analysis of *Xbp-1u* and *Xbp-1s*  
941 mRNAs. Total RNA was isolated and subjected to RT-PCR analysis using primers flanking the  
942 *Xbp-1* splice site. PCR products were resolved in a 3% TBE-agarose gel and visualized by ethidium  
943 bromide staining. *Rpl19* RT-PCR product was used as a loading control. Molecular size markers  
944 (nt) are indicated on the left. **(E)** Analysis of RPFs (Mock Ribo, Inf Ribo and Tunica Ribo) and  
945 RNASeq (Mock RNA and Inf RNA) mapping to *Xbp-1u* (NCBI RefSeq mRNA NM\_013842)  
946 showing, from top to bottom, mock 8 h (Mock), MHV 8 h p.i. (Inf) and tunicamycin treated  
947 (Tunica) cells harvested by flash-freezing. Reads whose 5' end maps to the first, second or third  
948 positions of codons relative to the annotated *Xbp-1u* CDS (blue rectangle) are indicated in purple,  
949 blue or orange, respectively. Yellow rectangles indicate the extended ORF in *Xbp-1s*. Green and red  
950 tick marks, and blue dotted vertical lines are as described in Fig 5C. Note that reads in the +2 frame  
951 downstream of the annotated stop codon (yellow peaks) are derived from translation of the *Xbp-1s*  
952 spliced isoform.



954 **Figure 6: Effect of MHV infection on unfolded protein response PERK-eIF2 $\alpha$ -ATF4 activity.**

955 17 Cl-1 cells were incubated in the presence of tunicamycin (2  $\mu$ g/ml) or infected with MHV-A59

956 (MOI 10) and harvested at 2.5, 5, 8 and 10 h p.i. (A) qRT-PCR of *Chop* transcripts normalized by

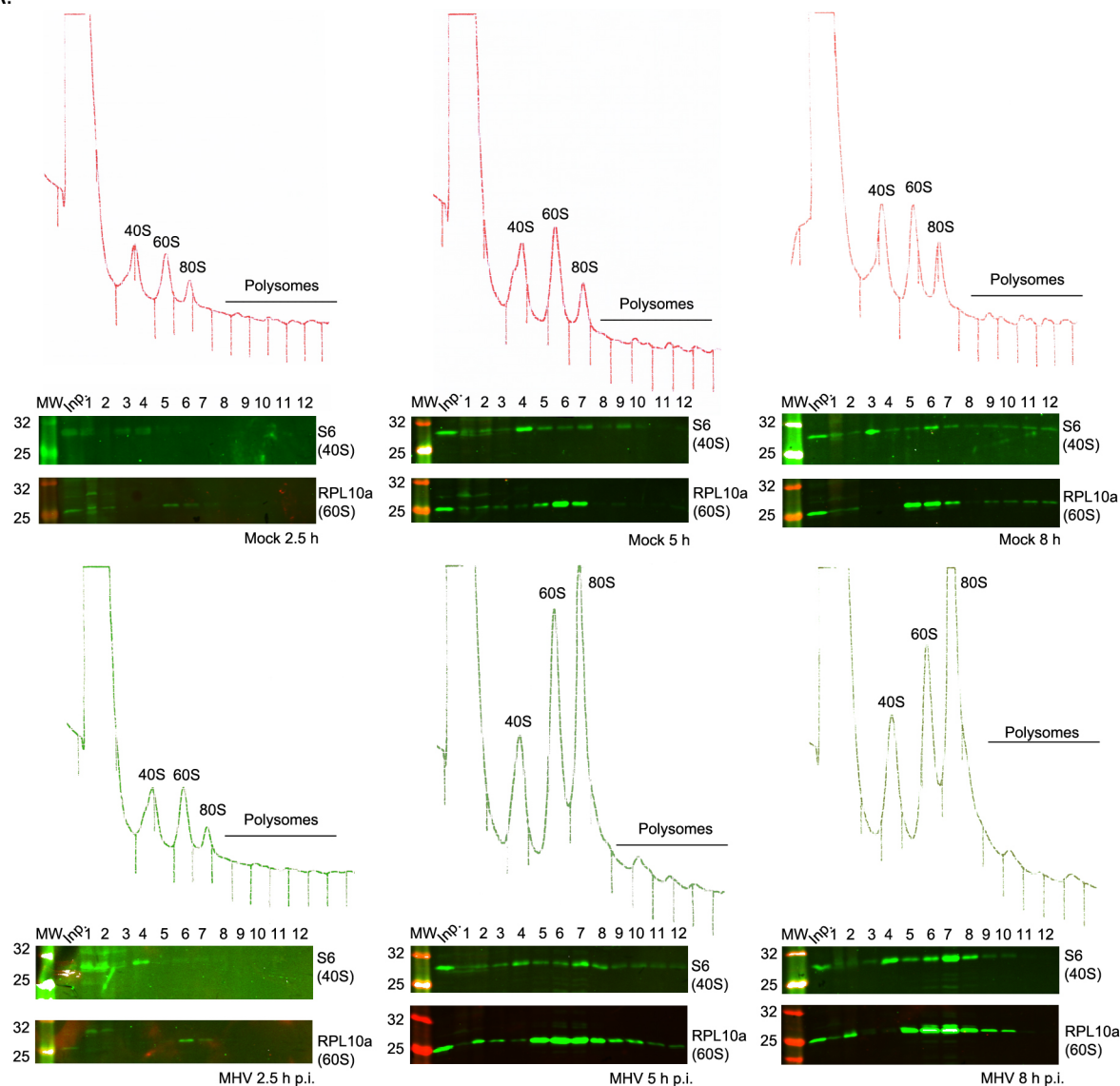
957 *Rpl19* transcript. (B) Cell lysates were separated by 12% SDS-PAGE and immunoblotted using

958 anti-ATF4, anti-p-eIF2 $\alpha$ , anti-eIF2 $\alpha$  and anti-N antibodies (green fluorescent secondary antibody).

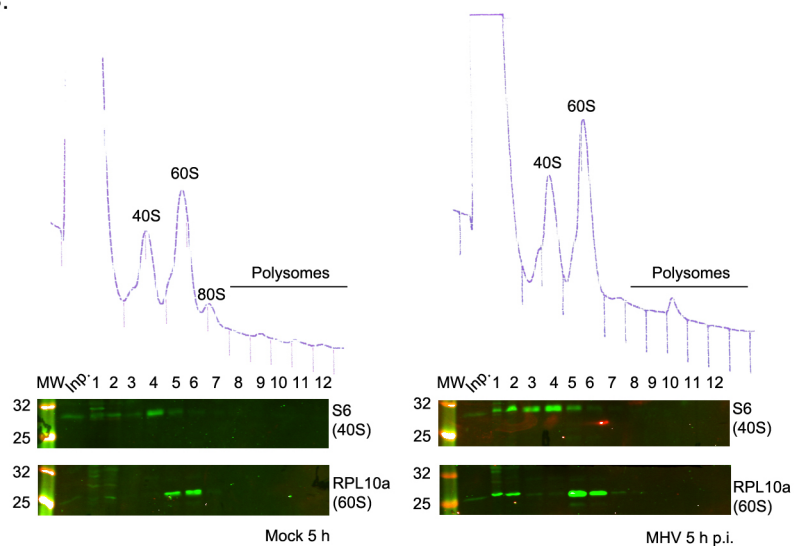
959 GAPDH was used as a loading control (red fluorescent secondary antibody). Molecular masses

960 (kDa) are indicated on the left. **(C)** Analysis of RPFs (Mock Ribo, Inf Ribo and Tunica Ribo) and  
961 RNASeq (Mock RNA and Inf RNA) mapping to *Atf4* (NCBI RefSeq mRNA NM\_009716)  
962 showing, from top to bottom, mock 8 h (Mock), MHV 8 h p.i. (Inf) and tunicamycin treated  
963 (Tunica) cells harvested by flash freezing. Reads whose 5' end maps to the first, second or third  
964 positions of codons relative to the annotated CDS (blue rectangle) are indicated in purple, blue or  
965 orange, respectively. Yellow rectangles indicate the *Atf4* uORFs. Green and red tick marks, and  
966 blue dotted vertical lines are as described in Fig 5C. **(D)** Analysis of RPFs (Mock Ribo, Inf Ribo  
967 and Tunica Ribo) and RNASeq (Mock RNA and Inf RNA) mapping to *Chop*, also known as *Ddit3*  
968 (NCBI RefSeq mRNA NM\_007837) showing, from top to bottom, mock 8 h (Mock), MHV 8 h p.i.  
969 (Inf) and tunicamycin treated (Tunica) cells harvested by flash freezing. Reads whose 5' end maps  
970 to the first, second or third positions of codons relative to annotated CDS (blue rectangle) are  
971 indicated in purple, blue or orange, respectively. Green and red tick marks, and blue dotted vertical  
972 lines are as described in Fig 5C. Note that reads in the +1 frame upstream of the annotated start  
973 codon (blue reads) are derived from translation of the *Chop* uORF (yellow rectangle).

A.



B.



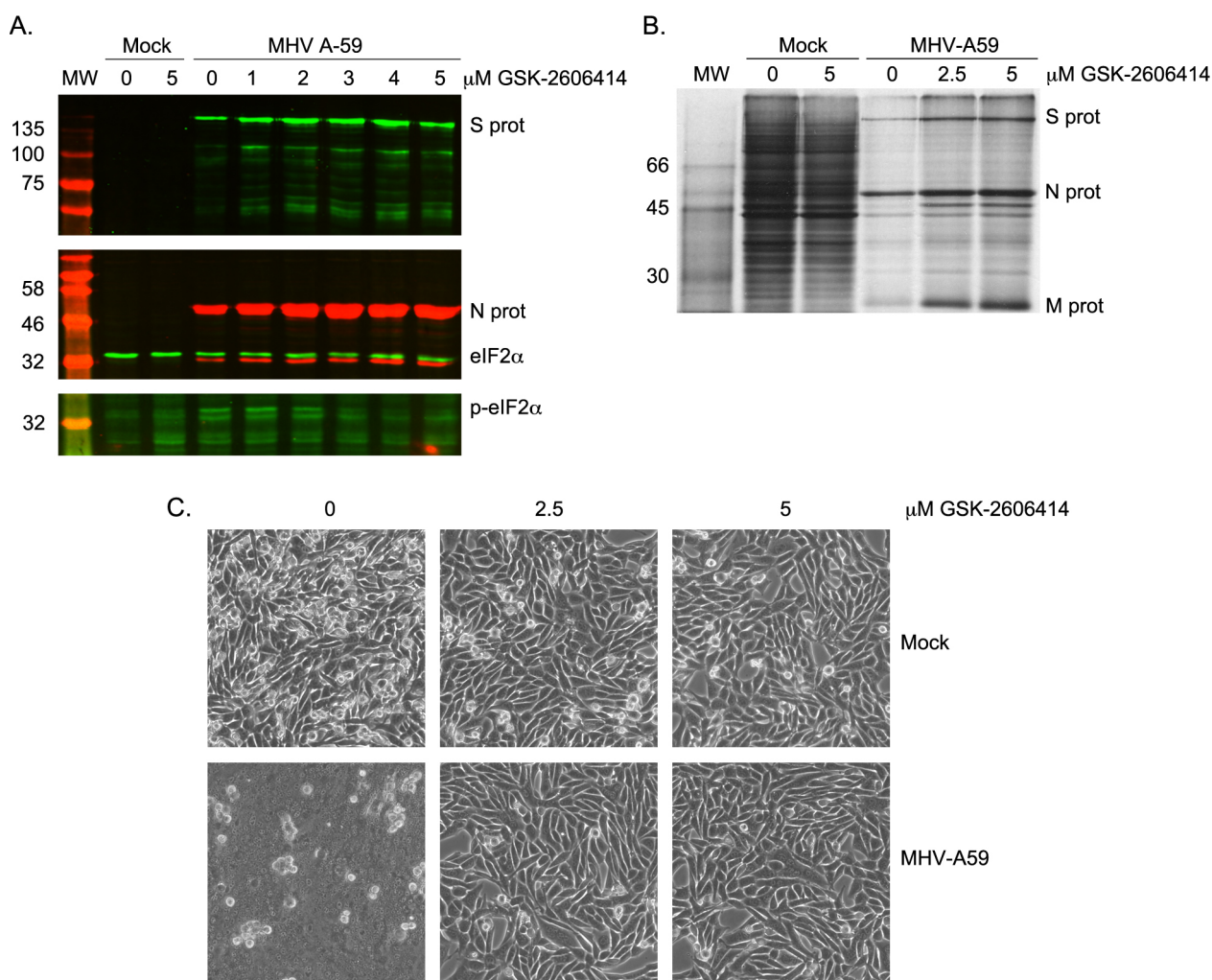
974

975

976

**Figure 7: Polysome profiling of 17 Cl-1 cells infected with MHV-A59. (A)** Mock-infected (upper panel) and MHV-infected (lower panel) 17 Cl-1 cells were harvested at 2.5, 5 and 8 h p.i.

977 Cytoplasmic lysates were resolved on 10–50% sucrose density gradients. Gradients were  
978 fractionated and fractions monitored by absorbance ( $A_{254}$  nm). Twelve [numbered] fractions were  
979 collected and proteins extracted, resolved by 12% SDS-PAGE and analysed by immunoblotting  
980 using the indicated antibodies (anti-S6 as 40S marker, anti-RPL10 as 60S marker, anti-N and anti-  
981 S). (B) Mock-infected (left panel) and MHV-infected (right panel) 17 Cl-1 cells were harvested at 5  
982 h p.i. in high-salt lysis buffer (400 mM KCl) and analysed as described above. Molecular masses  
983 (kDa) are indicated on the left. Lane "Inp" contains whole cell lysate.



985 **Figure 8: Effect of GSK-2606414 on MHV-infected cells.** (A) 17 Cl-1 mock and MHV-infected  
986 cells were treated with 1–5  $\mu$ M of the PERK-inhibitor GSK-2606414. GSK-2606414 was added to  
987 the cells immediately after the virus adsorption period was completed and maintained in the  
988 medium until cells were harvested 5 h later. Cell lysates were separated by 12% SDS-PAGE and

989 immunoblotted using anti-S, anti-p-eIF2 $\alpha$  and anti-eIF2 $\alpha$  (green fluorescent secondary antibody),  
990 and anti-N sera (red fluorescent secondary antibody). Molecular masses (kDa) are indicated on the  
991 left. **(B)** 17 Cl-1 cells infected with MHV-A59 and treated with 0, 2.5 or 5  $\mu$ M of GSK-2606414  
992 were metabolically pulse-labeled with [ $^{35}$ S]Met for 1 h at 5 h p.i. Cells were lysed just after pulse  
993 and subjected to 10% SDS-PAGE followed by autoradiography. **(C)** Representative images of  
994 mock and MHV-infected cells at 5 h p.i. treated with 0, 2.5 or 5  $\mu$ M of GSK-2606414.  
995